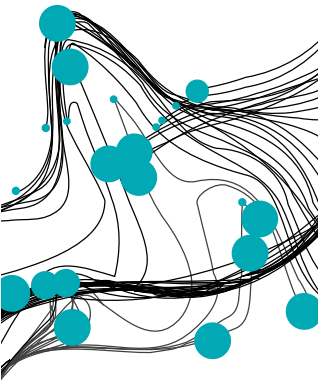

RAM ROBOTICS AND MECHATRONICS

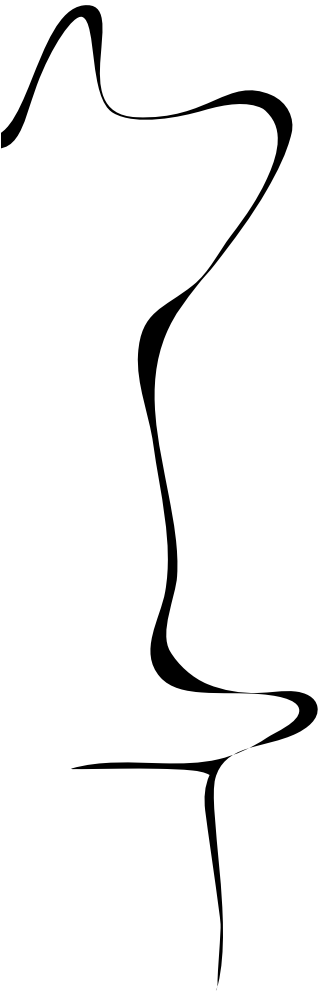

DESIGN AND DEVELOPMENT OF VARIABLE IMPEDANCE ACTUATOR USING A MULTI AXIS MOTOR

V. (Vignesh) Palani

MSC ASSIGNMENT

Committee:
prof. dr. ir. S. Stramigioli
dr. V. Groenhuis, MSc
dr. J. Dasdemir

August, 2023

046RaM2023
Robotics and Mechatronics
EEMCS
University of Twente
P.O. Box 217
7500 AE Enschede
The Netherlands

UNIVERSITY OF TWENTE. | TECHMED CENTRE
UNIVERSITY OF TWENTE. | DIGITAL SOCIETY INSTITUTE

Acknowledgment

First and foremost, I would like to express my deepest gratitude to my supervisor, Dr. Vincent Groenhuis. His constant support and wise guidance played a key role in the completion of this thesis. I truly appreciate his systematic way of helping me find solutions by asking the right questions. Every discussion with him was a valuable learning opportunity. No matter when I reached out, he was always there to help with any questions about the research or thesis writing.

I'd also like to extend my sincere thanks to my committee chair, Prof. Dr. Ir. S. Stramigioli, and Dr. J. Dasdemir for willingly being part of the evaluation committee.

My family has always been there for me throughout this journey, and I can't thank them enough. A special thanks goes to my sister, Archana. Her belief in me and her encouragement, especially during tough times mean the world to me. Akka, you will forever be my rock.

A big thank you to my friends as well, who were by my side every step of the way. They've been there through the ups and downs, lifting me up when I was down, and celebrating every achievement, big or small. A heartfelt shoutout to Avni, Manaswini, and Nilay — you all made me feel at home, even when I was far from it.

Lastly, ella pugazhum iraivanukke.

Thank you.

Abstract

This research focuses on improving the interaction between robots and their environment by merging two key technologies - Variable Impedance Actuators (VIAs) and multi-axis motors. The former helps the robot to move more like humans while being flexible and safe. The latter offers control over multiple rotational axes, facilitating multi-dimensional movements and increasing the degrees of freedom in robotic systems. However, despite their individual benefits, each of these technologies has challenges, notably the torque limitations of multi-axis motors, evidenced in prior designs showing torque loss during simultaneous rotor actuation, and the complexity of VIA design. This study proposes the integration of these technologies to address the issues, resulting in a more compact, compliant, and efficient actuator system. Pivotal to this integration was the redesign of the motor's rotor, enhancing its size and augmenting the coil windings, thus boosting its torque. This research investigates various VIA categories, selecting the lever arm-based mechanism as optimal, and explores multi-axis motor designs, leading to a two-rotor configuration with a 50-teeth and 51-teeth rotor showcasing superior torque outputs. Furthermore, the study introduces the optimal spring type for the developed multi-axis VIA – a Ω-shaped spring crafted from specialized engineering plastics, which helps in achieving a better range of stiffness. As the research delves deeper into the design and integration of the developed VIA with the multi-axis motor, it becomes evident that this unique design is pivotal in ensuring a balance between stiffness and compliance. The adept control of actuator stiffness and position is facilitated by a MATLAB UI-based feed-forward control system. This empowers users to set the pivot point position, thereby influencing the VIA's stiffness directly. This innovative model stands as a testament to the immense potential of crafting a versatile VIA using a multi-axis motor without any significant reduction in precision. Streamlining the use of the multi-axis motor in this model not only reduces wiring intricacies but also unveils the potential of a simplified controller governing the entire mechanism.

Contents

Chapter 1

Introduction

In recent years, the field of robotics has seen significant and rapid growth toward providing more adaptable and realistic interaction between the user and the user environment. Previous research states that traditional actuators used in robotic systems are rigid and lack compliance [1]. To elaborate, they are often one-dimensional in terms of their usage, which hinders the ability of robots in terms of flexibility, making them risky to be used in unpredictable and dynamic environments [2]. This scenario led the research to a new era of robot design, concentrating on compliant robots using Variable Impedance Actuators (VIA). Specifically, in pursuit to make them safe and flexible in situations involving human-robot interaction. A VIA is a type of actuator that can vary its stiffness and damping similar to natural muscles improving the robot interaction [3].

Compliance in robotics is crucial to enable secured human-robot interaction. As it reduces the chances of accidents during various scenarios of physical contact, by enabling the robots to absorb the external impact. This allows safe interaction in shared workspaces. Apart from that, it also lets robots interact with several different objects, allowing for the lifting and manipulation of fragile or atypically shaped items as it can modify stiffness and compliance during dynamic interactions. Finally, it creates a wide range of opportunities for human collaboration with robots in various industries such as healthcare, teleoperations, and the energy sector requiring high precision, complex operations, and handling of a wide range of materials.

Similarly, the research on multi-axis motors plays a pivotal role in developing complex and dexterous robotic systems. These motors offer control over multiple rotational axes, facilitating the robots to have multiple degrees of freedom. This provides a wide range of actions, such as

reaching, gripping, and orientation adjustments, and improves mobility by controlling the motion of each axis separately. When compared to single-axis stepper motors of comparable sizes, such a motor offers various benefits such as smaller volume occupancy, much fewer cables, and enables the robot to perform multiple operations. This creates opportunities in applications such as industrial automation, mobile robotics, and humanoid robotics, where precise and agile motions are necessary.

1.1 Problem Overview

While multi-axis motors and VIA have individually made significant improvements, there still exist several problems in both these technologies. The challenge of improving the torque in the multi-axis motor, specifically when the multiple rotors are driven simultaneously hinders the efficiency and its potential applications because each rotor has to share the total power, which significantly affects the efficiency. Additionally, since the axes are coaxial, they tend to limit the spectrum of application.

Similarly, in the case of Variable Impedance Actuators(VIA), existing designs are often complex, the addition of an impedance control function requires additional components and a control algorithm that makes them bulky. In most cases, at least two motors are required to control the position and stiffness variation of the actuator. Also, changing the compliance settings takes time and limits the performance of existing VIAs.

Thus, this gives rise to an opportunity to integrate the multi-axis motor with VIA to tackle the above-mentioned existing issues. However, combining these two technologies while maintaining compliance and control precision poses various difficulties which this research focuses on.

1.2 Thesis Statement

In light of the challenges associated with existing multi-axis motors and Variable Impedance Actuators (VIAs), this study posits that integrating these two technologies—while enhancing the torque of multi-axis motors and simplifying the design of VIAs—will result in a more efficient, compact, and compliant actuator system. This newly designed system is anticipated to significantly improve the flexibility, safety, and usability of robotic systems, especially in areas requiring complex operations, high precision, and safe human-robot interaction.

1.3 Framework and Goals

By addressing the complexity of existing VIA designs and considering the torque limitations of the multi-axis motor, this study aims to develop an innovative solution that efficiently combines compliance and coordination in an integrated VIA with the multi-axis motor system.

To facilitate the design of a multi-axis motor integrated VIA, several essential aspects need to be studied and established. These include investigating different categories of VIAs and determining the suitable spring type for developing the design. Additionally, understanding the types of multi-axis motors and their key design parameters is crucial. Moreover, testing and controlling the stiffness actuator is necessary to ensure the desired performance.

Once these foundational aspects are successfully implemented, the multi-axis motor can be integrated with the VIA. The evaluation will focus on assessing the precision and smoothness of controlling the stiffness and position of the actuator using the multi-axis motor. This evaluation will provide insights into the overall performance of the integrated system.

This study aims to address the following research questions:

1. How do various categories of VIAs vary, and how can the "Adjusting load-spring transmission ratio" Variable Impedance Actuator be effectively integrated into the design of a developed multi-axis VIA?
2. How can the torque of a multi-axis motor be improved to facilitate its integration with a Variable Impedance Actuator?
3. How does the choice of shape and dimension of the developed spring influence the desired compliance and stiffness range of the developed Variable Stiffness Actuator (VIA)?
4. How can the stiffness and position control of the actuator be optimized using the multi-axis motor integration?

1.4 Outline

The report examines and summarizes the significant findings from past studies and analyses the new VIA design and multi-axis motor. Chapter 2 provides all related theories and research conducted within the scope of this study, and talks about the choice of VIA and multi-axis motors. Chapter 3 focuses on the design of the multi-axis motor, the reasons for those design choices, and their impact. Chapter 4 dives into the development and implementation of the

VIA, explaining the spring design, choice of material incorporation of the multi-axis motor, and identifying how to control the stiffness and position of the actuator. The experimental results are discussed in Chapter 5. Finally, in the 6th chapter, the conclusion, and recommendations are discussed.

Chapter 2

Literature Review

This chapter covers the intensive overview of existing literature and past studies on VIA and Multi-axis motor technology. As the research delves into incorporating the VIA with the multi-axis motor, the literature focuses on the various types of VIAs and their state-of-the-art development. Also, it highlights the development of multi-axis motors and their underlying principles.

2.1 Variable Impedance Actuators[VIAs]

Variable Impedance Actuators (VIAs) are believed to play a pivotal role in creating a safe ecosystem, it facilitates collaboration between humans and robots by enhancing robotic manipulation, bringing it closer to the capabilities of human beings [4]. Furthermore, Vanderborght, B. et al.[4] also suggest that traditional actuators built on the principle of 'stiffer the better', while providing quick response and accuracy to the change in setpoints often limit the adaptability due to the consequences caused by its mechanical properties such as mass, inertia and stiffness on the control of the entire robotic system. Hence, VIAs developed by drawing inspiration from the bio-mechanics of animals offer a higher degree of versatility and interactive capabilities of robots [5].

As described in [6], an overview of the different categories of VIAs is provided, and a classification is proposed based on the principles through which the variable stiffness and damping were achieved. The main categories of VIAs include active impedance by control, inherent compliance, damping actuators, and inertial actuators. Figure 2.1 visually represents the categories of VIAs.

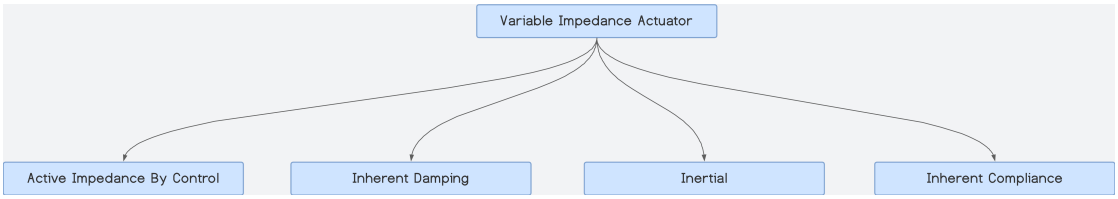

Figure 2.1: Categories of VIAs

The Active Impedance by control does not have any intrinsic compliant element but rather tries to replicate the response of an impedance solely by using software control [7]. The software tries to make the actuator more flexible by obtaining sensor data to change the behavior which provides high accuracy to the changes. However, it is often complex to design, and since it depends solely on the controller, no energy can be stored as these controllers have limited bandwidth [8]. Figure 2.2 shows a closed-loop control process of active impedance by control, the reference input determines the desired behavior, and the controller minimizes the difference between this and the sensor-measured system state by sending appropriate control commands to the plant, resulting in a desired impedance behavior.

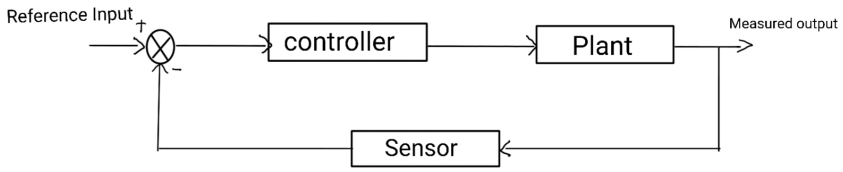

Figure 2.2: General principle behind Active impedance by control

While Inherent Damping Actuators consist of the passive element which allows natural damping of the system, Vanderborght, B. et al.[6] gives an insight into the influence of the field of eddy currents, fluid dynamics, friction, and controlled rheology on the implementation of these actuators. Figure 2.3 depicts a few possible Inherent damping actuators. The major drawback of an Inherent damping actuator is that the design requires high scrutiny as it dissipates the energy due to its damping components, which causes stability issues [9].

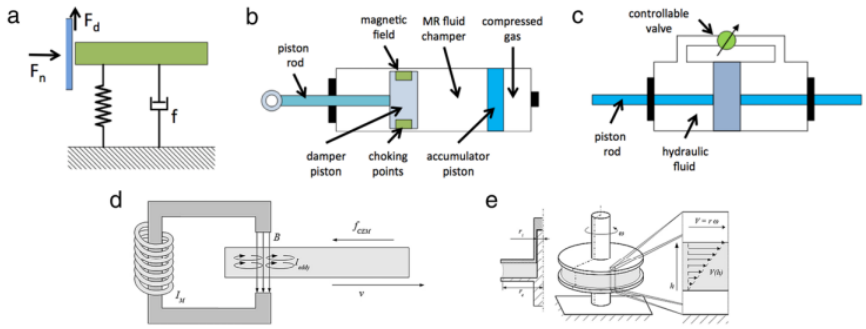

Figure 2.3: Examples of Inherent damping actuators (a) friction, (b) Magneto-rheological, (c) variable orifice fluid damper, (d) eddy current, (e) laminar viscous damping

In the case of Inertial Actuators, uses inertial components vary the stiffness and store the energy in kinetic form. According to Nelson, C.A. et al.[9], it often is very bulky and stores enormous energy, due to which it may have limited bandwidth capacity.

Finally, the Inherent Compliance Actuator is very similar to damping actuators, although here it allows natural compliance of the system. This nature is beneficial because it provides high bandwidth due to the compliance component, which makes it capable of absorbing sudden impacts and enhances energy storage [10–12]. Inherent compliance can further be divided into two subcategories as fixed compliance actuators such as Series elastic actuators(SEAs)[13], and Variable stiffness Actuators(VSAs) [6]. Figure 2.4 depicts the categories of Inherent Compliance Actuator.

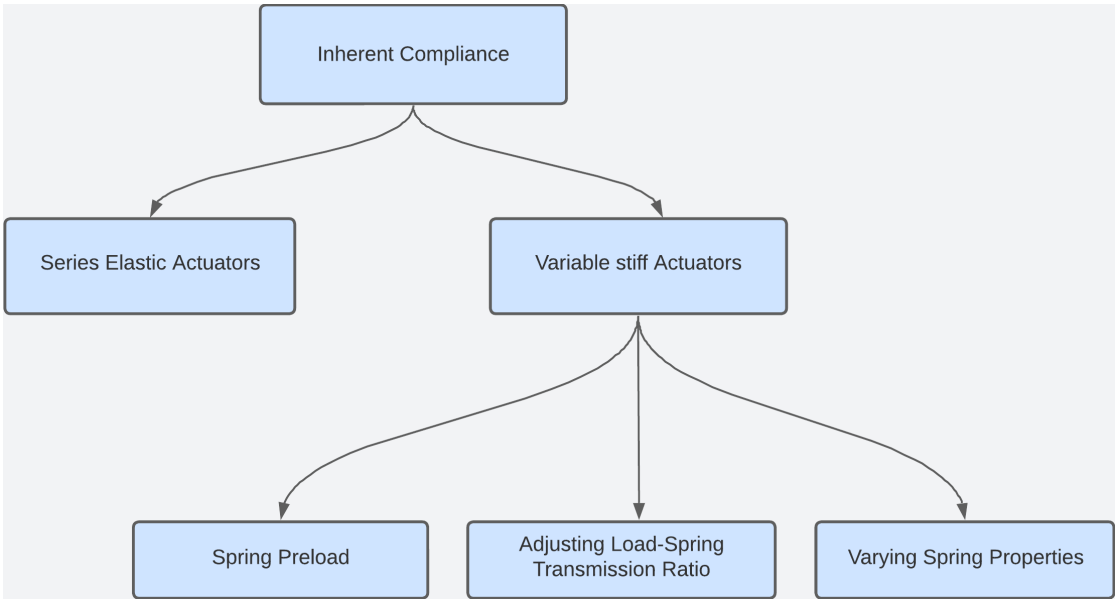

Figure 2.4: Hierarchical structure of Inherent Compliance Actuators [6]

In the case of traditional SEA, the stiffness property of the actuator generally cannot be changed automatically during the operation. The properties depend on the selection of the spring and can be manipulated only by pausing the operation. To overcome the limitations of SEAs, VSAs were developed. The major advantage of VSA is that the elastic components used in the actuator can absorb the sudden shock to the system from the environment and can intensify the output power by using saved energy [14]. Thereby improving the safety scenario, especially in Human-robot interactions.

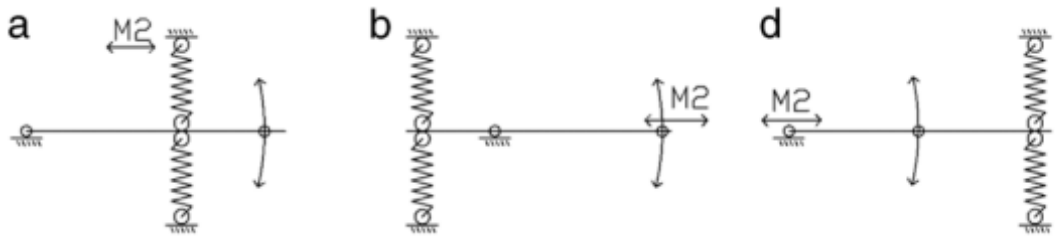

Figure 2.5: (a) By changing spring position, (b) By changing the position of force acting on the system, and (c) By changing pivot position [4]

In the spring pre-load category, the stiffness of VSA can be changed by pre-loading or changing the pre-tension of the spring. While the Adjusting Load-spring ratio category achieves the same without having to change the pre-tension of the spring, it rather varies the transmission ratio

between the output link and the spring. This in theory also reduces the energy consumption [6]. The different types of Load-spring ratio categories are depicted in figure 2.5. Unlike the previous categories, Varying spring material properties can also be pivotal in achieving efficient compliance with the system [15].

2.1.1 Previous work

Research over the years has shown various benefits of using a VSA type of VIAs such as a wide range of stiffness, simplicity in design, higher bandwidth, etc. [16–19]. Malosie, M. et al. [20], developed RotWWC-VSA which uses antagonistic configuration to create non-linear stiffness. The actuator consists of two nonlinear equivalent springs actuated by two motors to control the equilibrium position and stiffness. However, antagonistic configuration VSA creates convolution in terms of control design as it has constraints on the energy efficiency of the system due to the configuration.

Mechanically adjustable compliance and controllable equilibrium position actuator (MACCEPA) [21], varies the stiffness based on pre-tensioning the springs. This pre-tensioning influences the torque, thus controlling the spring constant parameter to vary the stiffness. MACCEPA Concept was used in various applications such as biped and Exoskeleton. However, since the motor has to handle the spring loads the efficiency of the VIA is affected. To address this issue variable lever spring ratio mechanisms were introduced. The concept of mechanically adjusting the stiffness increases the flexibility as well as decreases the cost because the energy used to adjust the stiffness does not add to the force that the spring is exerting [6].

In [22], the University of Twente developed a VIA, which is based on a linear spring connected with a lever arm. The lever arm length can be varied because of which different spring stiffness can be achieved. By changing the internal configuration, the output stiffness can be regulated with the effective use of energy. In the case of AwAS [23], the spring location is changed instead of varying the lever arm length to achieve variable stiffness. Jafari, A. et al. [24], propose to change the control of the range of stiffness by changing the pivot point of the lever mechanism in AwAS-II. This change allows VIA to provide a force amplification ratio ranging from zero to infinity. The varying pivots reduce the control complexity and minimize the power consumption of the motor.

Several methods have been identified for the smooth change of the pivot position, which increases the efficiency of VIA. In [25], a Cam-shaped lever arm mechanism is used to move the pivot point as shown in Figure 2.6 of Compact-VSA.

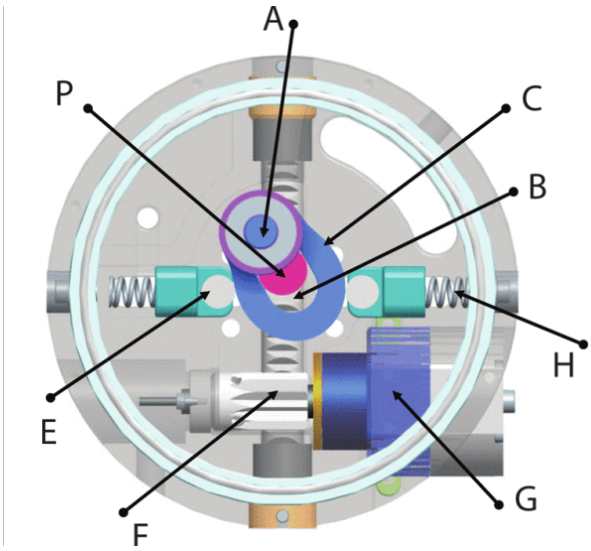

Figure 2.6: Lever arm mechanism with variable pivot point of Compact-VSA [25]

It is seen that the most efficient method to change the lever arm ratio is to move the pivot point along the lever[26]. Hence in the vsaUT-II, the pivot point is changed by using a ring gear of diameter 'd', and a pivot gear with a pitch diameter 'd/2'. The pivot is connected to the pivot gear at a distance of 'd/4' from its center as shown in figure 2.7. This mathematical relation between the gear allows the pivot to follow a trajectory of a straight line while the pivot gear rotates around the ring gear. Multiple variations of differential for this mechanism are discussed in [27].

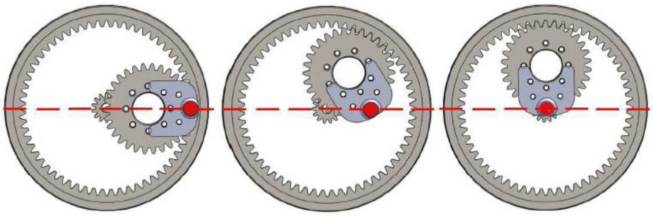

Figure 2.7: The mechanism to move the pivot along the lever in a straight line [26]

Jafari, Amir et al. [28], discuss the different kinds of springs that can be used for making VIA. This paper provides an overall understanding of the parameters of the spring and their effect on the design of VIAs. One key relationship governing the behavior of springs, especially in relation to their stiffness, can be expressed by Euler bernouli's beam principle as:

$$k = \frac{E \cdot b \cdot d^3}{4 \cdot L^3} \tag{2.1.1}$$

This formula elucidates that the spring stiffness (k) is directly proportional to the cube of its thickness (d).

Furthermore, [29], Barrett, E. et al. gives an insight into the different materials that can be used in making a spring for a VIA. The results demonstrate that engineering plastics, such as various polymers, exhibit high stiffness and, consequently, superior energy storage capacity compared to metal springs. The usage of such polymers will also reduce the spring weight and can be commercially manufactured with ease.

2.2 Multi-axis Motors

Previous research has shown Various configurations of Multiple axis actuation being explored for Brushless Direct current (BLDC) motors, and stepper motors. These include designs such as Dual rotor and single stator designs, Dual stator and single rotor designs, Dual rotor, and stator designs, and spherical motor designs.

In [30], spherical rotors are used to achieve 3 perpendicular rotational degrees of freedom(DOF). However, such configuration demands complex controllers to control the 3 DOF independently (Figure 2.8.

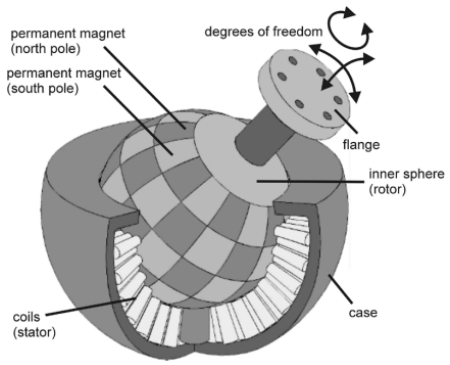

Figure 2.8: Design of Spherical Motor [30]

While in the case of Dual rotor and stator design configuration [31], the two rotors can be controlled as two independent motors, offering two rotational degrees of freedom. The disadvantage is that because of the presence of two stators two separate windings are required which causes the need for two separate controllers.

The third configuration, a dual stator single-rotor motor [32], offers one linear degree of freedom and one rotational DOF. The two stators are distributed with three-phase windings along radial and axial axes separately to produce one rotary and one linear motion (Figure.

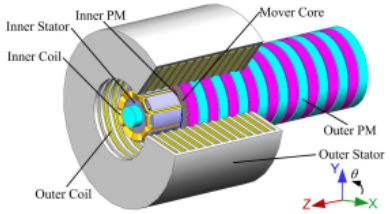

Figure 2.9: Design of Dual stator single rotor motor [32]

Taking into account various configurations, Groenhuis, V. et al. [33] proposes a state-of-the-art multi-axis stepper motor, which is a triple rotor, single stator configuration, as a compact and efficient solution for actuating multiple DOF within a single device. The three shafts are coaxial, which allows them to be mechanically independent(Figure 2.10. The motor shafts are controlled individually by providing a different number of steps to each rotor. The high phase count improves the consistency of the torque, and the single-winding configuration allows easy control over the DOFs.The limitation of such a motor is that since the power of the motor has to be distributed among the rotors, the torque reduces by 49% when the three rotors are actuated together.

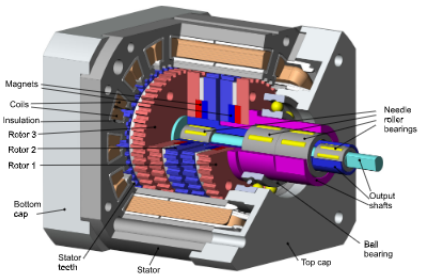

Figure 2.10: Design of Multi-axis stepper motor [33]

Furthermore, [34] Groenhuis, V. et al. improve the stator configuration to create more winding space and increase the stator teeth similar to a bipolar stepper motor. This allows for the incorporation of higher pole pairs which facilitate precise control over the position of the rotor.

2.3 Conclusion

In conclusion, the literature review highlights significant advancements in the field of Variable Impedance Actuators (VIAs) over the years. In particular, most of them focus on improving stiffness range and reducing control complexity, especially in the context of human-robot interaction. In recent times, there have also been efforts to combine the different categories to enhance the capabilities of the VIA.

It is evident that most VIAs typically require multiple motors to control both the stiffness and position. However, this research aims to achieve both stiffness and position control using a single motor, specifically the multi-axis stepper motor. Considering the constraints posed by the multi-axis stepper motor, the VSA type is chosen as the basis for developing a VIA integrated with the multi-axis stepper motor.

Furthermore, before creating such an integrated VIA, the design parameters of the multi-axis motor are modified to obtain better individual torque performance. This modification indirectly improves the torque when the rotors are driven simultaneously.

By integrating the advantages of the VSA and the multi-axis stepper motor, this research seeks to overcome the limitations observed in existing systems and develop an efficient and versatile actuation system. The following chapters will delve into the design, development, and experimental validation of the integrated VIA and multi-axis motor system to address the research questions.

Chapter 3

Design of the Multi-Axis Motor

This chapter presents an in-depth exploration of the design, developement and control of the multi-axis motor, a specialized type of electric motor that is capable of driving multiple rotational axes simultaneously.

The research builds upon the work of Groenhuis, V. et al. [33], acknowledging the limitations of the existing multi-axis motor operation, especially in the context of the torque output when the multiple axes are driven simultaneously. It is noted that when three shafts are driven simultaneously, the torque generated is 42% lower than the average torque generated when each axis is actuated individually. Similarly, when two axes are driven simultaneously, the torque reduces by 29% compared to when each axis is actuated separately. Despite these observations, the research suggests the potential for optimizing internal dimensions to enhance the torque.

To improve the understanding, 3D designs are used to visually conceptualize the motor assembly, thus illustrating the impact of the design decisions on the motor's operation. This approach aims to optimize the torque output while maintaining the benefits of multi-axis motors, such as a compact and integrated control system.

Considering the VIA's requirement to have precise stiffness and position control, the multi-axis motor is constrained to two axes. This adaptation facilitates higher torque and provides an integrated control system.

3.1 Stator

In their research, Groenhuis et al. ([33]) use a stator that is structured in a seven-phase star configuration, facilitating the actuation of multiple rotors. Notably, their design includes 14 stator poles, arranged as two poles per phase, with each pole comprising three teeth. This arrangement gives a total of 42 teeth, evenly spaced around the circumference of the pole to facilitate precise movements. Each coil in their design includes 50 turns of insulated coil winding. However, due to the symmetrical arrangement of the seven coil pairs, the coil length becomes significant, potentially leading to high resistance, which may negatively impact the motor's torque. Moreover, the equal interval spacing of the 14 poles reduces the number of coil turns for each stator pole.

In subsequent work, Groenhuis et al. proposed modifications to their stator design to improve rotor position control and minimize measurement errors [34]. They maintained the seven-phase star configuration but reduced the number of stator arms to seven, with each arm having seven teeth spaced equidistantly. This design increases the total number of teeth to 49 and also enhances the winding space for each coil. These modifications enhance the electrical properties of the motor, specifically by reducing the winding resistance. This reduction allows for an increase in the current supplied to the motor, which consequently increases the torque. Additionally, the improved winding space facilitates better heat dissipation. The star configuration allows for the use of sinusoidal waveforms for rotor actuation, which reduces electromagnetic interference (EMI). By minimizing EMI, the accuracy of the motor's control is improved. However, it's important to note that this stator design was applied to a single-axis motor configuration.

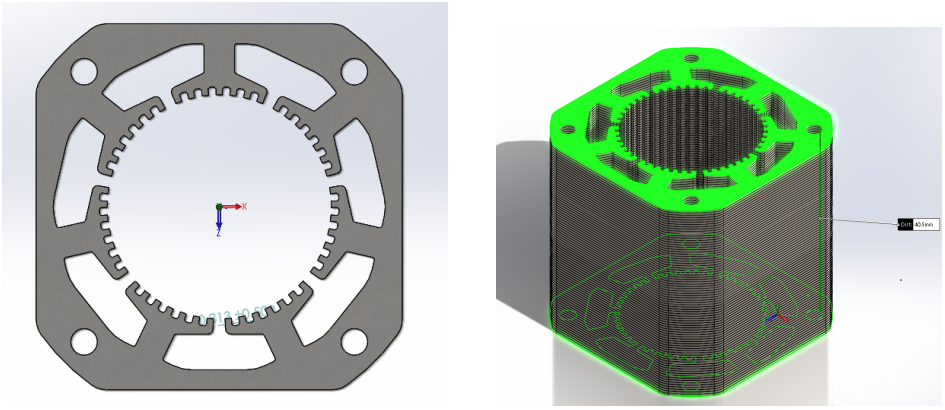

(a) Stator design **(b)** Stacked stator core

Figure 3.1: 3D model of the stator

However, contrary to the previously mentioned research, the current paper focuses on the development of the multi-axis motor which employs a seven-arm stator configuration. The stator core in this design measures 42 X 42 mm^2, with each stator layer having a thickness of 0.5 mm. The overall height of the stator is 40.5 mm, which allows for the stacking of 81 stator layers with identical teeth configurations to facilitate dual rotor actuation. The seven poles are evenly spaced around the stator, with each tooth on an arm set 7.059 degrees apart, forming a diameter of 25.9 mm. A 3D model of this design was developed using SolidWorks, as shown above in Figure 3.1.

3.2 Rotors and shafts

The motor's design includes two rotors, one with 50 teeth and the other with 51. The selection of the number of teeth on the rotors is contingent upon the number of teeth present on the stator. Given that the stator has 49 teeth, the number of teeth on the individual rotor should not be a multiple of 7. Additionally, the total count of teeth on two rotors combined should not be divisible by 7 [34]. This requirement ensures a suitable distribution of rotor pole pairs, as the number of teeth on the stator influences them. These interactions play a crucial role in generating the force that drives the motor's shafts, hence directly influencing the torque. Too small or too large gaps between adjacent stator arms could lead to an uneven distribution of magnetic forces, complicating the independent control of the two rotors.

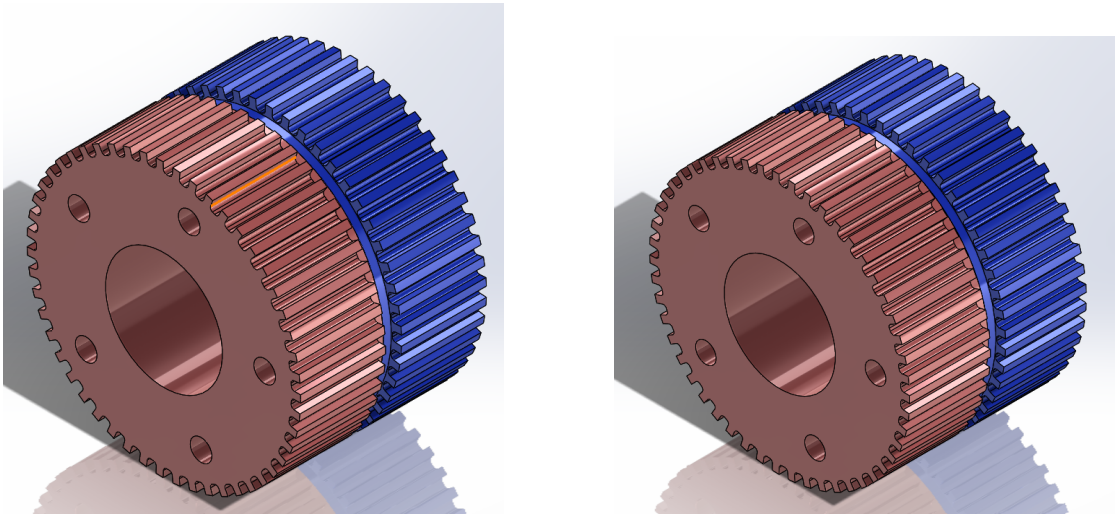

(a) **(b)**

Figure 3.2: (A)3D model of the 50-teeth rotor (B) 3D model of the 51-teeth rotor

Each rotor in the design has a diameter of 25.8 mm and a height of 17.5 mm. They are composed of two identical halves, each measuring 8 mm in height. The rotor design includes a magnet of dimensions $\varnothing$23.8 X 1.5 mm^2 and a 13 mm diameter hole to accommodate independent shafts, as shown above in Figure 3.2. The rotor magnets are arranged to repel the adjacent rotors. The effective teeth width of the rotors is 0.68 mm at a radius of 12.9 mm. The two halves of the 51-teeth rotor are assembled together at an offset of $360°/(2.51) = 3.529°$, while for the 50-teeth rotor is $360°/(2.50) = 3.6°$. By increasing the height while keeping the rotor diameter constant, the magnetic field of the stator will interact with the rotor more strongly along the vertical axis. This alteration is expected to result in a significant increase in torque, addressing the limitations of the previous design, while ensuring there is no significant increase in the size of the motor to achieve better torque.

The design incorporates coaxial shafts for the rotors. The inner coaxial shaft has a diameter of 5 mm, while the outer shaft measures 12 mm in diameter. MR85ZZ ball bearings are used to separate the inner shaft from the outer one. The outer shaft, meanwhile, is positioned between the 61801 ball bearings (Outer Diameter: 21 mm, Inner Diameter: 12 mm) and the motor's bearing holder. A gap of 1 mm is maintained between the two rotors to avoid frictional loss. The complete assembly of the motor is illustrated in Figure 3.3.

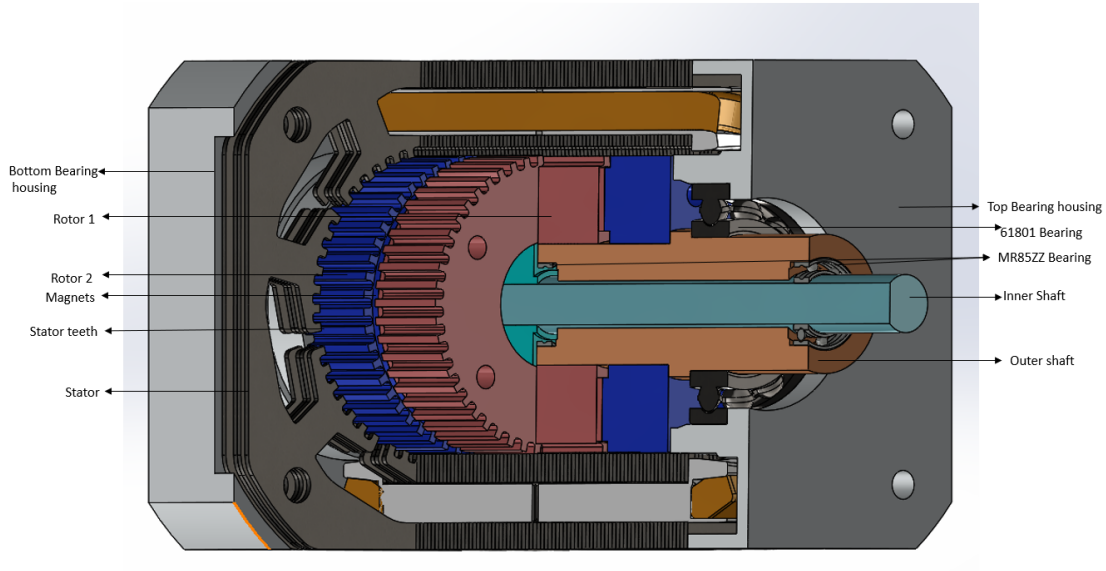

Figure 3.3: Cut out view of the developed multi-axis motor

3.3 Control

The controller used for controlling the multi-axis motor allows the user to control the position and velocity of each rotor of the multi-axis motor independently. The control system is based on the Teensy 4.0 microcontroller unit (PJRC.COM LLC, Sherwood, OR, USA), which utilizes a high-performance NXP i.MX RT1062 processor. This processor is equipped with an ARM Cortex-M7 core running at 600 MHz [33]. the specification allows the microcontroller to compute the waveforms to ensure precise control over the multi-axis motor.

This microcontroller operates synchronously with the 7 Half H-bridges to facilitate pulse width modulation. It allows the precise adjustment of the multi-axis motor's speed and positioning, which are crucial for managing the stiffness of the VIA. Figure 3.4 depicts the controller used to control the motor.

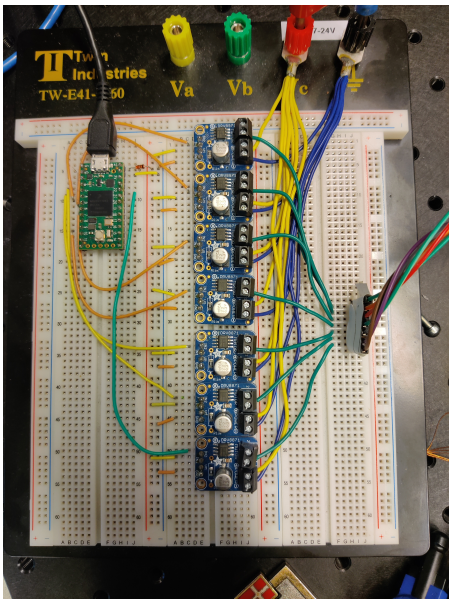

Figure 3.4: Controller of the multi-axis motor [35]

3.4 Prototype

The components of the 3D assembled multi-axis motor were later drafted as CAD drawings to manufacture them. The stator is made by laser cutting 0.5 mm thick electrical steel plates, which were later stacked and bonded with a back lack. The passage for the rotor to be placed between the stator was precisely machined to a $\varnothing$ of 25.9 mm. The stator arm is then winded by a copper coil of thickness 0.33 mm with 75 turns in each with one end of the coils centrally

grounded while the other end is individually provided to the controller. The rotors were also machined with the same material as the stator. A neodymium magnet was integrated between the two halves of the rotor. The shafts were machined from stainless steel and bearings were installed in close tolerances between the shafts to eliminate any possible play. The entire rotor assembly is later placed within the stator with the help of the bearing on the outer shaft and the bearing holders, which are held together with four screws as shown in Figure 3.5.

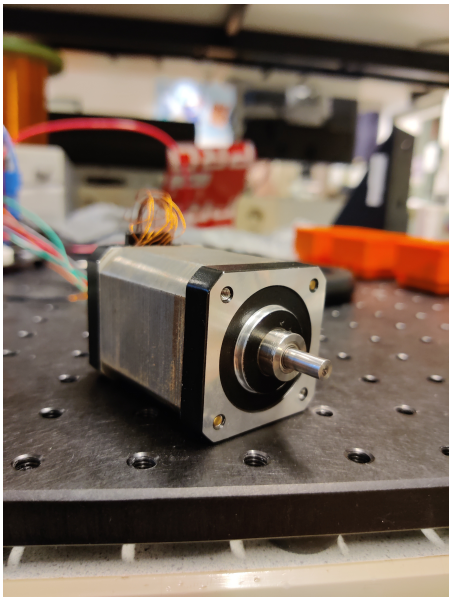

Figure 3.5: Realization of the prototype

Chapter 4

Develpoment and Implementation of the VIA

After conducting comprehensive research, detailed in section 2, a Variable Stiffness Actuator (VSA) with a lever arm mechanism was chosen over other subclasses of VSAs. The lever arm VSA stands out due to its unique benefits, which include flexibility, adjustability, and safety. Although VIAs designed to combine other types might offer more control, they often introduce added complexity to the system.

Specifically, lever-arm mechanisms are well-suited for this actuator type due to their ability to alter the internal configuration based on changes in the transmission ratio. This aids in preserving the internal storage capacity needed for stiffness variations.

This chapter will showcase the overall design choices made to create the VIA. It will further discuss the operating principle of the developed VIA when integrated with a multi-axis motor. Additionally, the control algorithm used to efficiently change the actuator's stiffness will be discussed.

4.1 Design of VIA

4.1.1 Lever-Arm mechanism

In 2.1.1, it is noted that the best way to modulate the transmission ratio to adjust the stiffness is by moving the pivot point. In this case, the developed model uses this mechanism to design the VSA and is similar to the mechanism developed in [29]. One end of the lever is connected

to the spring while the other end of the lever is free which takes the external load and enables movement around the pivot. The pivot is allowed to move in a straight line along the lever to vary the transmission ratio, thus changing the output stiffness of the system.

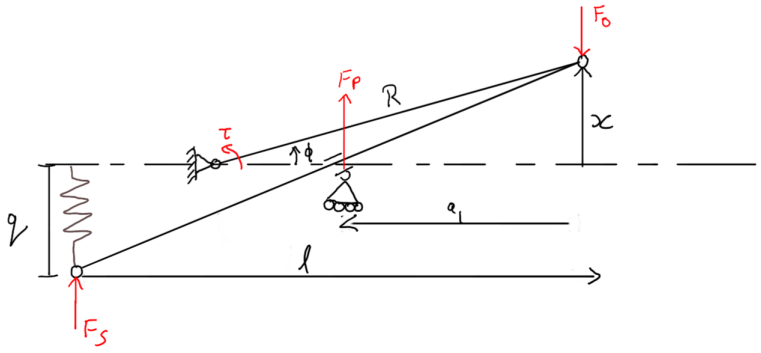

Figure 4.1: VSA design based on the deflection of the lever on the output side

Figure 4.1 illustrates how the lever-arm ratio adjusts the stiffness of a mechanism. The applied rotational torque τ deflects the lever by an angle ϕ about the crank R. The deflection 'x' results from this rotation and can be calculated as x= R·sin(ϕ). Due to this rotation, the spring connected at the other end experiences an elongation 'q', generating a spring force F_s.

In this system, 'l' represents the total length of the lever. The position of the pivot, denoted by 'a_1', is the distance from the free end of the lever to the pivot point. It is considered that the values of 'a_1' and 'l' remain unaffected by changes in 'ϕ' as long as the angle 'ϕ' and the '$\frac{q}{l}$' ratio stay small, as determined by the developed design of the lever arm.

Due to the output force and the spring force, an internal load develops at the pivot point, resulting in a force F_p. At equilibrium, the sum of all forces acting on the system equals zero, meaning the forces generated by the applied torque, the lever arm, and the spring must balance each other out.

$$F_s + F_p - F_o = 0 \tag{4.1.1}$$

The VSA uses a linear spring for the purpose. Hence, the internal forces on the lever-arm mechanism are provided as follows[29],

$$F_s = k_s \cdot q \tag{4.1.2}$$

where k_s is the spring constant of the spring and q in terms of x is given as q = $\frac{l-a_1}{a_1} \cdot x$

$$F_o = \frac{l - a_1}{a_1} \cdot F_s \tag{4.1.3}$$

where F_o is the output force acting on the lever.

$$F_p = F_o - F_S = (\frac{(2 \cdot a_1) - l}{a_1}) \cdot F_s \tag{4.1.4}$$

The output torque τ of which deflects the lever is,

$$\tau = F_o \cdot R = \left(\frac{l - a_1}{a_1}\right) \cdot k_s \cdot \left(\frac{l - a_1}{a_1}\right) \cdot R \cdot \sin(\phi) \tag{4.1.5}$$

For a small angle of deflections $\sin(\phi) \approx \phi$ Therefore, the output stiffness due to the lever arm mechanism can be said as,

$$K = \frac{\partial \tau}{\partial \phi} = (\frac{l - a_1}{a_1} \cdot R)^2 \cdot k_s \tag{4.1.6}$$

Hence, from 4.1.6 it is seen that the output stiffness created due to the lever-arm mechanism depends on the pivot positions and is linearly proportional to the spring constant. The output stiffness can be adjusted by changing a_1.

4.1.2 Spring

In the design of a spring for a lever-arm-based Variable Stiffness Actuator (VSA), maximizing energy utilization and enabling a broad deflection range for varying transmission ratios is crucial. Numerous types of springs have been deployed in passive compliance-based VSAs over the years, such as helical, torsional, and leaf springs [36–38]. However, the majority of lever-arm-based VSA designs predominantly utilize pre-tensioned springs. Pre-tensioning places the spring under continuous tension or compression, which consequently impacts the spring's maximum deflection potential.

Addressing this, Barrett, E. et al. proposed an Ω-shaped spring, a leaf spring variant, that maximizes energy storage by extending the active length of the spring [29]. Uniquely, this spring is not pre-tensioned, which enables it to be loaded in both directions. This is an improvement over the conventional pre-tensioned spring system, where two springs, each counteracting the other, would be required to achieve the same dual-direction load capacity. Another advantage of Ω-shaped springs not being pre-tensioned is their potential for increased

durability which creates a potential to store maximum energy. The maximum energy storage capacity of the spring is given by:

$$W_b = \frac{1}{9} \cdot \frac{(\sigma_{\max})^2}{2 \cdot E} b \cdot h \cdot l \tag{4.1.7}$$

In this equation, '$\sigma_{\max}$' refers to the material property, 'E' is the young's modulus of the material, while 'l', 'b', and 'h' denote the length, breadth, and height of the spring, respectively.

In this research, the Ω-shaped spring was adapted for optimal compatibility with the VSA design. This decision was driven by the spring's compact design, absence of pre-tensioning requirement, and maximum energy storage capability. Equation 4.1.7 illustrates that the spring design can be optimized by manipulating the spring's volume and material selection. A variety of Ω-shaped springs were developed through a trial-and-error approach using Solidworks and then represented as 3D models. Initially, the overall height and width of the spring were restricted to a maximum of 60 mm each. Then, the cross-sectional area of the spring was adjusted to effectively exploit the shape for energy storage [39]. Numerous iterations of the shape were optimized within these constraints, and each was tested based on the compliance obtained. The 3D models were converted into STL files within Solidworks and subsequently 3D printed. Figure 4.2 presents the optimized spring model that was integrated into the VSA design. The shape and size were carefully selected to visually illustrate the novel concept of integrating a VSA with a multi-axis motor.

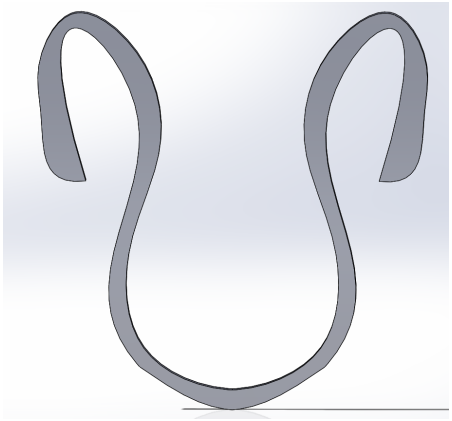

Figure 4.2: 3D model of the Ω- shaped spring

Upon finalizing of the spring design, mounting points were created with a 3 mm diameter hole to secure the spring to a frame. This arrangement aids in connecting the lever and the spring.

Additionally, a 5 mm diameter hole was extruded at a height of 13 mm from the spring's central base. This feature allows for equal actuation of the spring when the lever is deflected in either direction.

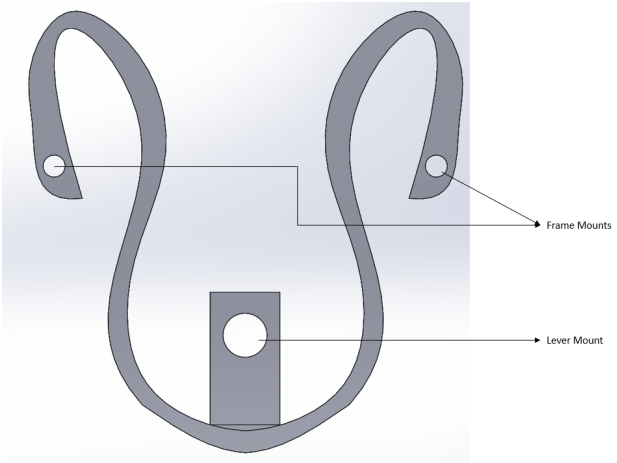

Figure 4.3: Fixtures of the Spring

4.1.2.1 Choice of Spring Material

Generally metal springs are widely used as spring materials in the case of VSA designs but they are often difficult to manufacture if a complex shape is required. Engineering plastic has shown promising development in various applications in robotics[40]. Similarly [29], shows how springs made with polymers are beneficial. They are lightweight materials and make it easy to manufacture complex designs while providing similar stiffness characteristics as that of metal springs.

A key component of the design was the choice of materials for the developed variable impedance actuator (VIA). Due to their distinct mechanical characteristics and adaptability to ensure a wide range of stiffness, co-polyester (CPE(+)) and polycarbonate (PC) were chosen. While PC has a σ_{max} of 68 MPa and Young's modulus of 2.64 GPa, CPE(+) has a tensile stress at yield σ_{max} of 48 MPa and Young's modulus of 1.52 GPa [41].

In conclusion, our material selection process was strategic, driven by the goal of understanding how different materials, such as CPE(+) and PC, influence the performance of the developed VIA.

When comparing springs of similar sizes, the CPE(+)-based spring demonstrated significantly lower stiffness, making it an ideal candidate for VIA construction. However, it is crucial to note that the selection of spring stiffness largely depends on the application. For instance, in heavy

load-lifting environments, a PC-based spring might be more suitable. On the other hand, a CPE(+)-based spring might be more apt for scenarios involving human-robot interactions due to its lower stiffness, hence ensuring safety and compliance.

Consequently, for the subsequent analysis in the implementation of the VIA, the 7.5mm thickness Ω-shaped springs were chosen for comparison due to their low stiffness and applicability in a broader range of operations.

4.1.3 Compounded Sun and Planet Epicyclic Gear Mechanism

When utilizing a motor to actuate the pivot motion, it's essential to convert the rotary motion of the motor shaft into translational motion. This conversion allows the pivot to move along the lever slot in a straight line. As previously discussed in section 2.1.1, this conversion can be achieved using a sun gear, a planet gear (also referred to as the pivot gear), and a ring gear [26].

The change in the pivot point is facilitated by using a ring gear of diameter 'd', coupled with a pivot gear of pitch diameter 'd/2'. The pivot is connected to the pivot gear at a distance of 'd/4' from its center. This specific ratio ensures that the pivot moves in a straight line, translating the rotary motion of the motor into the desired linear motion.

However, the gear ratio for such a mechanism will be very high, due to which high torque might act on the mechanism to affect the pivot position. This can be further improved by using an epicyclic gear mechanism. But in such mechanism, the planet gear typically meshes with both the ring gear and sun gear, which leads to wear of the teeth due to the load acting on them also causing high vibration.

Hence, compounded sun and planet epicyclic gear mechanism is proposed. In this case, the sun gear meshes with an idler gear which is in turn compounded with the planet gear. Due to the motion translated to the idler gear, it makes the planetary gear mesh with the fixed ring gear. This reduces the gear ratio and also the vibration caused by the system significantly. Thus, giving a higher speed for the transmission to pivot, which is a desired property for a VIA.

The ring gear is chosen to be of ⌀60 mm, while the pivot gear has an ⌀of 30 mm, and the compounded gear is of ⌀20 mm, which meshes with the sun gear of ⌀10 mm. Based on the above ratios the pivot of ⌀6 mm is placed at 15 mm from the pivot gear($(\frac{1}{4})^{th}$ of diameter of the ring gear). This ratio allows the pivot to cover the same distance as that of the ring gear. Since the pivot can move linearly by 60 mm, a wide range of output stiffness 'K' of the VIA can be achieved. Figure 4.4 shows the 3D model of the compounded epicyclic gear mechanism used for the developed VIA.

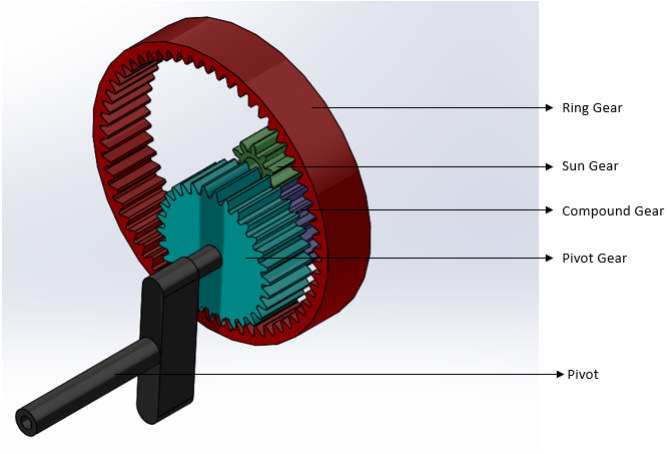

Figure 4.4: 3D model of epicyclic gear system with the pivot

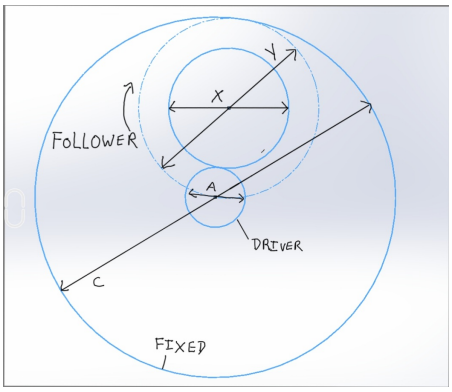

Figure 4.5: Princlple of epicyclic gear system

From Figure 4.5 the gear ratio of such a system can be calculated based on the following[42],

$$D = 1 + \frac{(X \cdot C)}{(Y \cdot A)} \tag{4.1.8}$$

where 'D' is the gear ratio, 'X' is the diameter of the compound gear, 'C' is the diameter of the ring gear, 'Y' is the diameter of the planet gear, and A is the diameter of the sun gear. From the above equation, the current model's transmission ratio is 5:1.

The transmission of the planet gear to the pivot transmission is non-linear, it follows a sinusoidal wave. The pivot reaches the maximum position from the lowest point by half the rotation of the planet gear. If the planet gear further rotates, the pivot starts moving down towards the lower position. Although this will create complexity while developing an algorithm

for controlling the stiffness of the VIA. Hence, a housing is created to hold the compounded epicyclic gear mechanism within it while allowing the gear to rotate only one-half cycle as shown in Figure 4.6. While designing it was ensured that the casing does not have any friction against the casing.

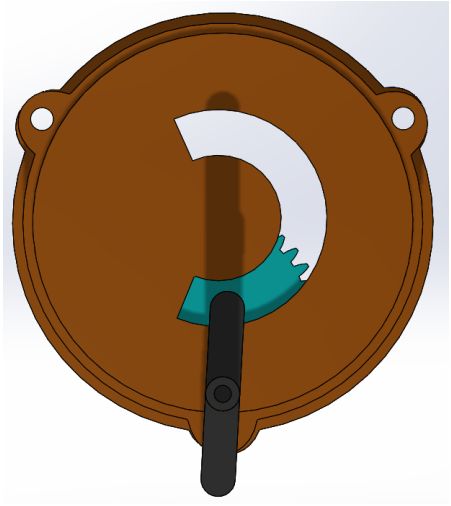

Figure 4.6: Housing of the compounded epicyclic gear mechanism

The entire transmission mechanism including the pivot is 3D printed by using Tough PLA to ensure high durability and is a very easy material to print due to its good bed adhesion and minimal warping capacity. The pivot was printed with a steel rod of ⌀3 mm placed inside them to improve the load-bearing capacity of the pivot.

4.1.4 Frame Design

The frame design is a critical component of the developed Variable Impedance Actuator (VIA). It not only facilitates the integration of the VIA with the multi-axis motor for precise position control over the lever but also holds the spring and lever in their optimal positions. Thus, the frame plays a pivotal role in the overall mechanism's functionality.

The lever, which measures 20 mm x 7.5 mm x 100 mm, is designed with a symmetrical internal slot. This slot extends 60 mm high and 6.3 mm long through the structure, enabling the pivot to move up to 60 mm along the lever, as depicted in Figure 4.7. At the free end of the lever, a circular extension with a diameter of 10 mm has been designed to facilitate the connection of an output shaft.

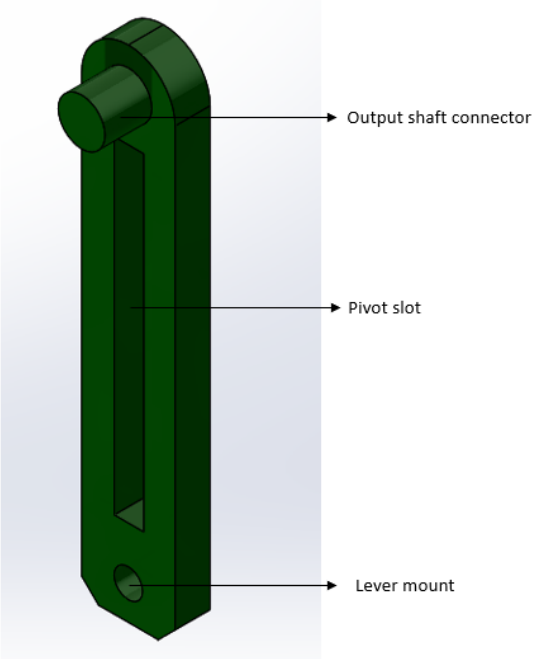

Figure 4.7: 3D model of lever

The frame was designed keeping in mind the dimensions of the spring, while also providing enough space for the spring to deflect by a minimum of 10 mm on both sides. The overall dimension of the frame is 95 mm X 95 mm X 25 mm. Based on the hole-to-hole distance of 52 mm between the frame mount of the spring, two support structures were developed to maintain the symmetry of the spring and lever when placed in the frame. The shaft support is provided as a cut-out ⌀of 8 mm at a height of 70 mm with a center distance of 84 mm between two holes to connect the frame to the outer shaft of the multi-axis motor.

To allow the pivot to move in a straight line through the lever while also enabling the lever to move around the pivot, a fixed structure of about 120 mm in length similar to the length of the lever, allowing the pivot to travel was extruded from the base of the frame maintaining the distance of 8 mm from the spring to allow the lever to move freely.

At the frame's top ends, a 4 mm diameter cut-out is designed to affix the compounded epicyclic gear to the frame. This feature allows relative movement between the epicyclic gear and the frame, ensuring a smooth, linear pivot adjustment regardless of the lever's position due to frame rotation. To mitigate the deflection of the epicyclic gear mechanism, a sturdy support structure is extruded from a point 40 mm high from the base and 30 mm apart from the

backside of the frame of thickness 5 mm. This arrangement ensures a firm transmission of the pivot.

The frame and lever were also designed using Solidworks to create the 3D model, Figure 4.8. which was later converted into an STL file to print the model. The material used to print was Tough PLA.

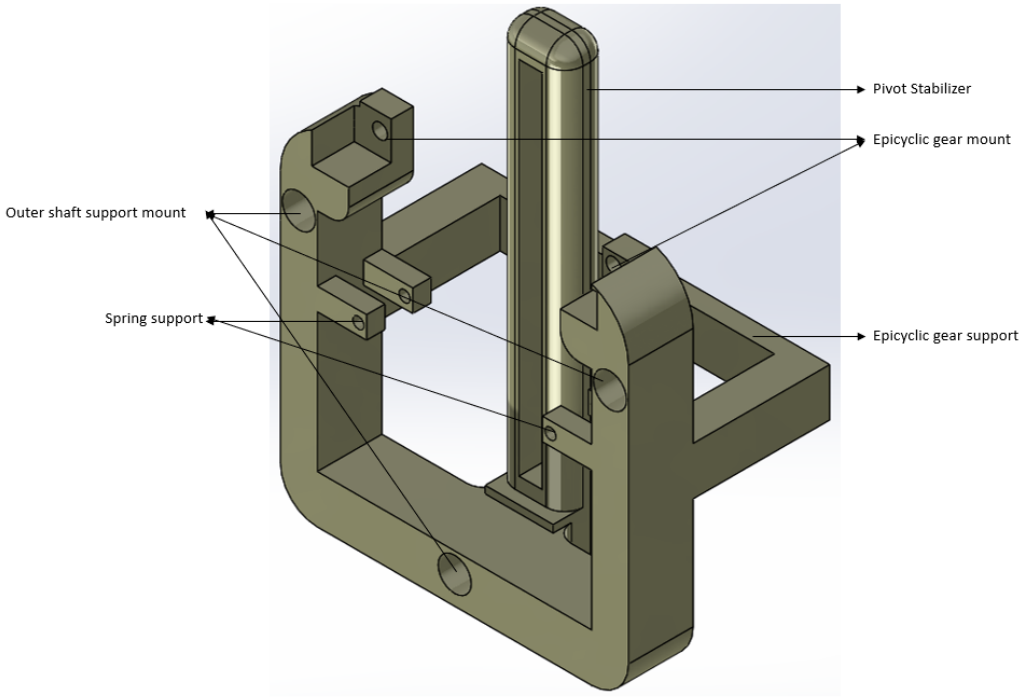

Figure 4.8: 3D model of frame

4.2 Working Principle of the Multi-axis Motor Integrated VIA

The spring of the mechanism is affixed to the frame's spring support. A lever establishes a connection between the pivot stabilizer and the spring, equipped with a degree of play to enable independent movement until the pivot traverses through the lever. The spring of the mechanism is secured to the support structure within the frame. A lever creates a connection between the pivot stabilizer and the spring.

Despite being positioned between the pivot stabilizer and the spring, the lever's connection is solely with the spring. The complete frame assembly is then attached to an external coaxial shaft, which has a diameter of 12 mm.

Simultaneously, the casing that houses the compounded epicyclic gear mechanism is fastened to the frame. This ensures that the pivot passes through both the pivot stabilizer and the lever. It also guarantees the constant support of the casing by the frame's epicyclic gear support, thereby mitigating any potential deflection of the pivot.

On the casing's opposite side, the mechanism's sun gear is fastened to the internal coaxial shaft of a diameter of 5 mm of the multi-axis motor. Consequently, as the multi-axis motor's internal shaft rotates, it enables the sun gear to transform the rotary motion of the shaft into the linear motion of the pivot, facilitating its linear movement of 60 mm.

Meanwhile, the frame handle as in Figure 4.9 is fixed to the outer shaft is utilized to transport the lever itself to the desired setpoint by maneuvering and spinning the frame. The outer shaft support of the frame handle is connected to the mounts on the frame. This system, integrating a VIA, employs a user-guided passive compliance approach. The lever's mechanical impedance is adjusted based on user-defined parameters to cater to the expected load at the setpoint. The position of the pivot point is manually set based on the application. By modifying the transmission ratio, the stiffness of the VIA is altered, enabling smooth load management.

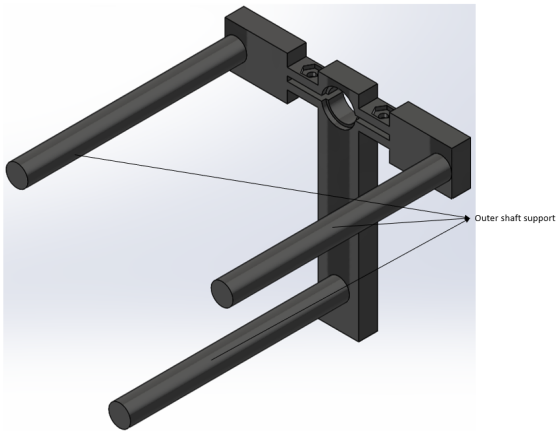

Figure 4.9: 3D model Frame handle

The external load exerted on the lever translates into an input force. Depending on this load, the external shaft generates appropriate torque for load movement. The pivot follows a consistent path along the lever's equilibrium position due to the relative motion of the epicyclic gear mechanism, facilitating manual stiffness adjustment.

The 3D assembly of the multi-axis motor and VIA is depicted in Figure 4.10. A Solidworks motion analysis confirmed the mechanism's operational efficacy and the absence of component

interferences. The final prototype realization is shown in Figure 4.11.

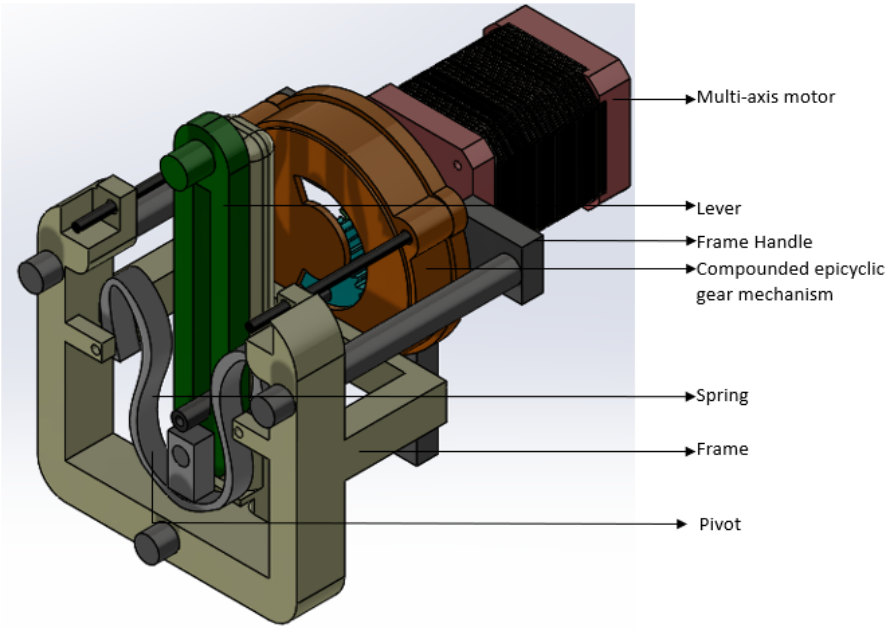

Figure 4.10: 3D model Multi-axis integrated VIA

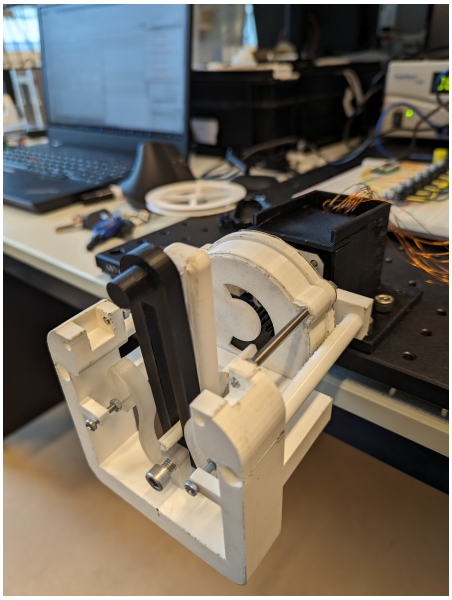

Figure 4.11: Prototype realization of multi-axis motor integrated VIA

4.3 Stiffness control of the VIA

This research focuses on creating a control algorithm to smoothly adjust the position of the pivot point to achieve a wide range of output stiffness of the developed VIA. Due to pragmatic reasons, this choice was taken, as creating a controller that controls the position of the lever and simultaneously adjusts the pivot position to control the stiffness, poses an enormous challenge. Especially in real-time interaction with the environment scenarios.

As outlined in section 3.3, the multi-axis motor's controller already facilitates the management of position, angular velocity, and power distribution to each rotor present in the motor. A Matlab App Designer User Interface (UI) developed by José Pratdesaba Lopez mediates this control, allowing users to manipulate the multi-axis motor. Communication between the controller and the computer host is made possible through a serial-over-USB interface. Figure 4.12 displays the design view of the MATLAB App UI for the multi-axis motor, which enables users to toggle between position control and velocity control for each rotor, as well as turn off the motor. The distribution of power to the rotors can be adjusted by dividing the pulse width modulation (PWM) to enable sharing of power between the rotors or to supply full power to a single rotor.

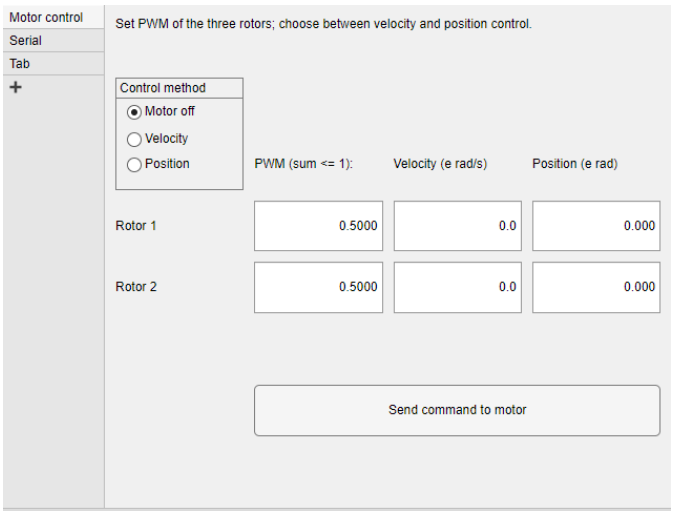

Figure 4.12: User interface of the multi-axis motor[43]

Since there are no feedback data available in the system, a feedforward control algorithm is used in this research. This term denotes an open-loop control system that uses a predictive model for adjustments. The model anticipates the system's responses to diverse inputs and adjusts the system before output measurement. The developed algorithm will later be incor-

porated as a slider in the MATLAB app UI, allowing users to set the pivot position using the slider as an input or the desired setpoint for the pivot. This enables the pivot to adjust even with minor changes in the slider's position.

To develop the feedforward algorithm, an understanding of the conversion of rotary to linear motion of the pivot through a compounded epicyclic gear mechanism is necessary. Section 4.1.3 reveals this transformation as non-linear and sinusoidal. With casing constraints, the maximum travel distance of the pivot allows the planet gear to rotate 180 degrees. Figure 4.13 provides a geometric representation of the pivot movement relative to the planet and ring gears.

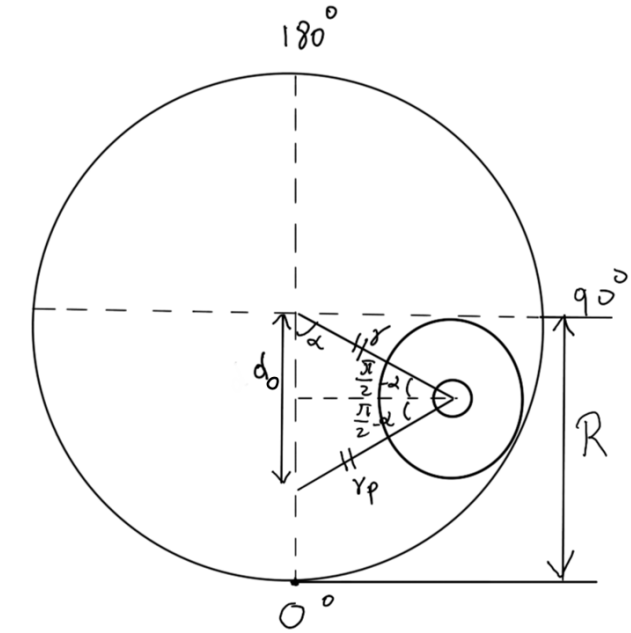

Figure 4.13: Geometrical representation of the Compounded epicyclic gear mechanism and the pivot

In Figure 4.13, 'R' represents the radius of the ring gear, 'r' represents the radius of the planet gear, 'r_p' represents the radius of the pivot, and 'd_o' represents the distance of the current pivot position from the origin at an angle of 'α' from the origin of the ring gear. It is noticed that the radius of the planet gear and the pivot is always equal hence, it can be said that,

$$\alpha = \arccos\left(\frac{d_o}{2 \cdot r}\right) \tag{4.3.1}$$

Equation 4.3.1 shows that with the planet gear's angle of rotation relative to the ring gear's

origin, it is possible to identify the pivot's d_o value. With 'R' and the known d_o, the pivot position can be determined. Given the 5:1 gear ratio between the sun gear and planet gear, the relationship between the number of sun gear rotations and the pivot's linear motion along the lever can be established. This relationship informs the creation of the feedforward algorithm, designed to efficiently adjust stiffness. The algorithm links to the UI's slider, where the pivot setpoint is provided as an input through the slider, and the inner coaxial shaft of the motor's rotation angle is provided as an output to the motor. A significant challenge of the algorithm lies in ensuring that it can differentiate its α values and distinguish between the quadrants where 0-180 degree lies.

Algorithm 1 shows the implementation in the MATLAB app UI, to control the stiffness using a slider.

Algorithm 1 Algorithm for controlling the stiffness of the VIA

```
Set distance of pivot from planet gear r as 15 mm and the radius of the Ring gear R as 30 mm
input_num = app.PivotpointSlider.Value                    ▷ Pivot setpoint
if input_num <= R then
    d_o = R - input_num
else
    d_o = input_num - R
end if
Print "do", d_o
alpha = acosd(d_o/(2*r))
if input_num > R then
    alpha = 180 - alpha
end if
degree = 5 * alpha
shaft_roterad = (degree * ((2 * pi * 51) / 360))
Print 'Degree of rotation as shaft_roterad
```

Figure 4.14, shows the Position control tab of the UI, providing instructions on how to set the pivot position using the pivot point slider.

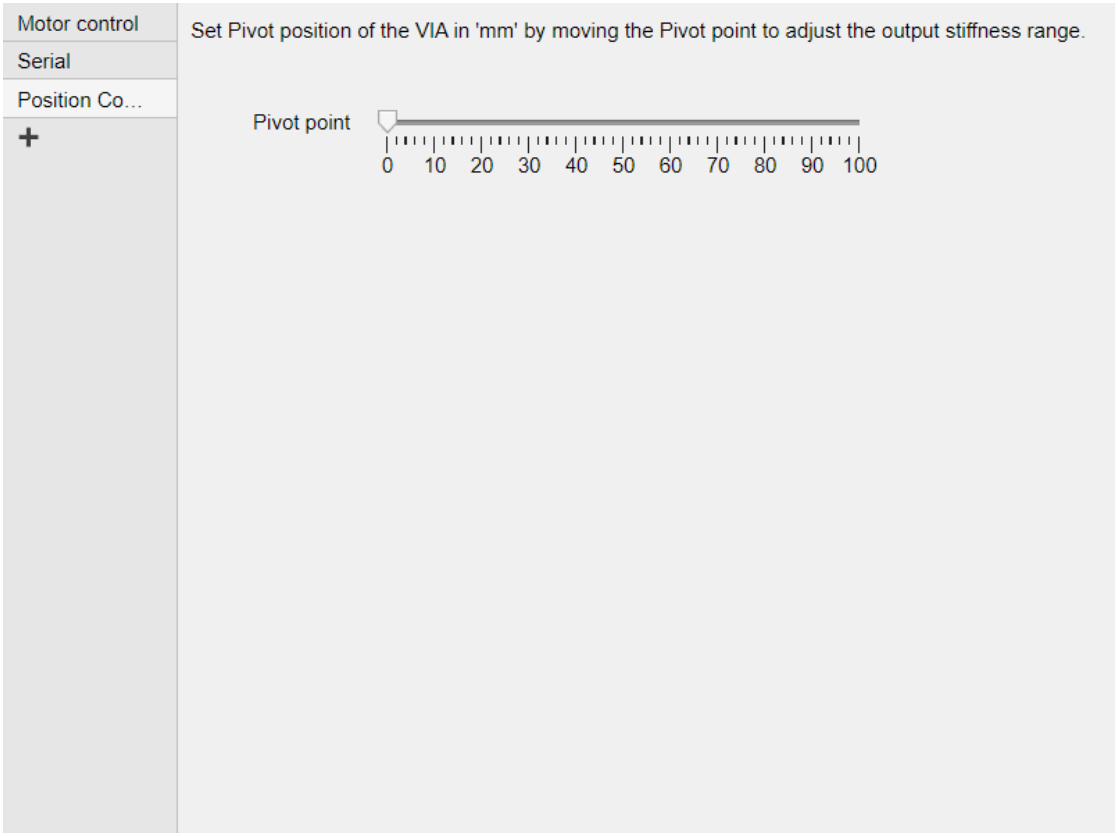

Figure 4.14: User interface of the position control page

Chapter 5

Experiments and Results

This chapter focuses on evaluating the concept of the designed multi-axis motor integrated VIA. This evaluation involves practical tests aimed at gaining an in-depth analysis of the performance of the integrated system.

Initially, the motor performance is evaluated in terms of the achievable torque at low speed and the maximum speed that the motor can achieve over each rotor of the motor, intended to measure the precision and responsiveness of the motor.

Subsequently, the spring element in the VIA is key to defining the impedance. The characteristics of the spring are studied for chosen materials, which provides insights into the ideal size for the developed VIA.

Finally, the range of output stiffness achievable by the developed VIA is examined. The output stiffness range is essential to understand as it provides a gauge on the VIA's adaptability to different environments and its tasks.

5.1 Motor Torque constant

The motor torque constant, denoted as k_t, is a key parameter of a motor that defines the relationship between the motor's current and the resulting torque. This constant is an inherent characteristic of the motor, determined by its design and construction.

In simple terms, the torque constant tells us how much torque the motor produces for a given current at constant voltage. The unit of k_t is typically Newton-meters per Ampere (Nm/A). A higher value of k_t implies that the motor can generate more torque for the same current. It

also allows an effective comparison of the torque produced by each rotor.

However, this torque increase is contingent on careful design choices regarding the thickness of the coil and the number of windings. These parameters need to be balanced to ensure that the increase in torque does not require a higher-than-nominal voltage or exceed the current capacity, which could compromise the overall performance of the motor.

Figure 5.1: Experimental setup for Motor torque constant

The Pulley-mass system (figure 5.1) is utilized to identify the torque constant of each rotor. The procedure is as follows:

1. A known mass is attached to a string wound around the pulley of radius 46mm which is attached to the motor shaft.
2. As the motor rotates, it lifts the mass and the torque on the pulley can be calculated from the mass, gravity, and radius of the pulley.
3. The current is measured directly from the power supply, as the motor does not have current sensors to measure the motor phase winding current. It is then reduced in small steps to identify at which value of current the rotor starts skipping steps. This value is

noted down. The current was manipulated by controlling the PWM of the motor.

4. This process is repeated for different currents and for weights to be lifted varying from 100g to 750g. The torque is calculated for each combination.

5. The torque value is calculated as the slope of the current vs torque graph.

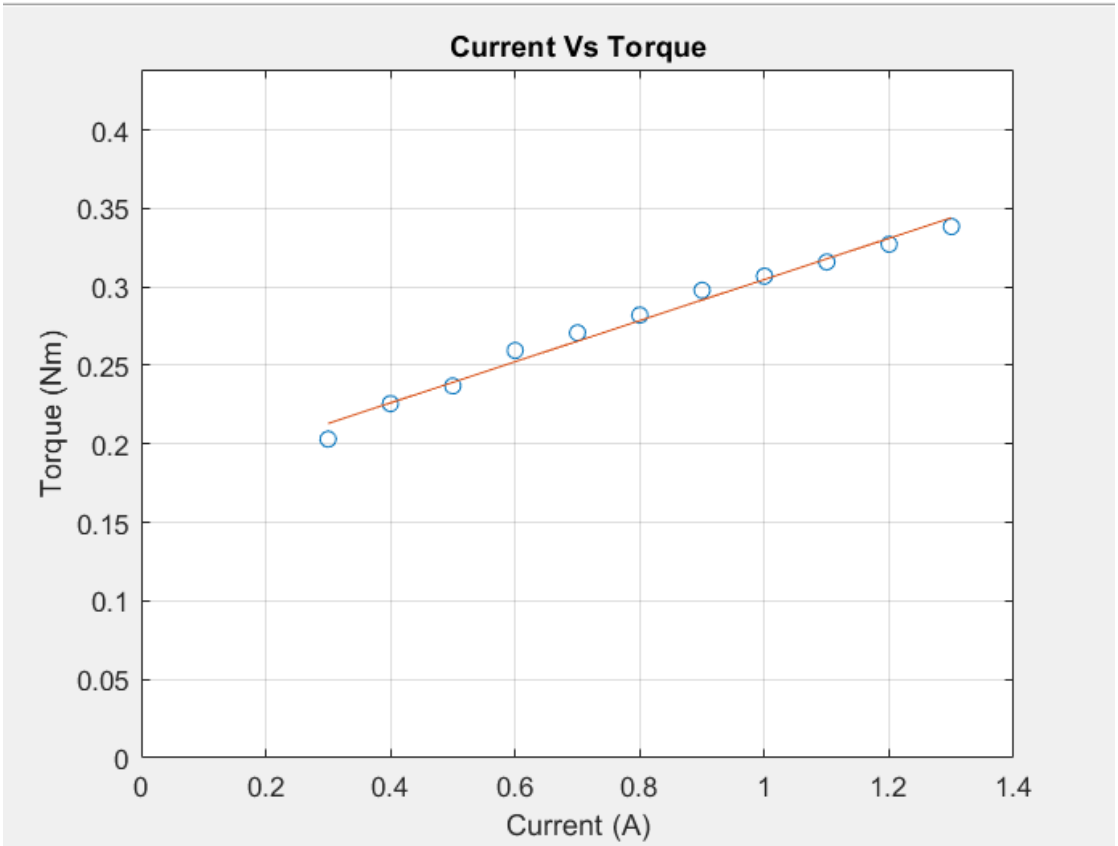

Figure 5.2: 50-teeth rotor Current-Torque graph

The above procedure was carried out for both rotors. Figure 5.2 shows the current-torque graph of the 50-teeth rotor. From the graph, it is identified that 'k_t" of the rotor connected to the inner shaft is 0.18 Nm/A. However, it is noted that from Figure 5.2 the slope does not pass through the origin because the Teensy 4.0 microcontroller is likely to consume a certain amount of current just to operate, even when it's not driving any load. This base current draw would create an offset in the graph.

5.2 No load speed

To calculate the maximum speed achieved by each rotor, an individual rotor was energized at a time with the full motor power provided solely to the selected rotor, applying a maximum voltage of 15V. This procedure was followed to ensure that the full power of the motor was available to the rotor being tested, thereby enabling an accurate measure of its maximum speed.

The motor's angular velocity was incrementally increased in steps of 100 rad/s. After each increment, the rotor was allowed to run at the newly established speed for at least 5 seconds to ensure smooth operation and stable measurements.

A key signal indicating that the rotor had reached its maximum speed was the occurrence of skipped steps in the shaft's rotation. When the rotor began to miss steps, it indicated that it had exceeded its optimal operating speed and was unable to keep up with the commanded speed, thus marking the maximum achievable speed.

With this procedure, the 50-teeth rotor shaft was found to attain a maximum speed of 5800 rad/s, which is about 1100 rotations per minute (RPM) at the given voltage. The 51-teeth rotor shaft attains a maximum speed of 1800 rad/s, which is about 380 RPM.

5.3 Spring stiffness

Having identified the desired shape and dimension of the spring through trial and error basis, as discussed in 4.1.2, the study involves examining the stiffness properties of the Ω-shaped spring. To provide a comprehensive perspective, springs are made of two materials as chosen in 4.1.2.1, each of varying thicknesses of 15mm and 7.5 mm respectively. The aim, of this analysis, is to determine which material and thickness combination offers better compatibility with the system designed.

Initially, each spring variant was simulated according to the expected environment of operation using Solidworks to identify the simulated spring stiffness constant value. The frame mount of the developed spring as shown in Figure 4.3 is fixed for simulation to represent reality and is subject to a normal load of a maximum 60 N at the left plane of the lever mount of the spring in order to allow the spring to deflect towards the right side. After this, a practical set of the same experiments was conducted for all the variants under controlled conditions. The load is provided at the point of contact of the lever connection to ensure the actuation of the spring represents the developed mechanism scenario.

A frame to clamp the spring similar to the original model is designed and is mounted sturdily on the mounting base. A screw is placed at the lever mount to which the load step of 50 grams is hung to the spring. Screws are used as the load by weighing and adding to a base plate. The weight is measured for each 0.5mm of deflection of the spring using a vernier caliper to ensure a sufficient amount of readings are obtained to identify the spring constant 'k_s'. The process is repeated for each variant of the spring.

A test frame is designed to mimic the clamping mechanism of the original model. This frame is robustly mounted onto the mounting base to ensure stability during load application. A screw is strategically placed at the lever mount to which the load is hung. The following procedure was adapted to test the spring stiffness (Figure 4.1.7),

Figure 5.3: Experimental setup to test the Ω-shaped spring

1. Loads of 50 grams increments are hung on the spring via the lever mount. This loading is implemented by using screws as weights, which are added to a base plate.
2. The weight of the screws is carefully measured for each 0.5 mm deflection of the spring.
3. Measurements of the spring deflection are carried out using a vernier caliper. This ensures that a sufficient iteration of readings is obtained to accurately calculate the

spring constant by calculating the slope of the graph.

4. This testing process is repeated for each variant of the spring printed.

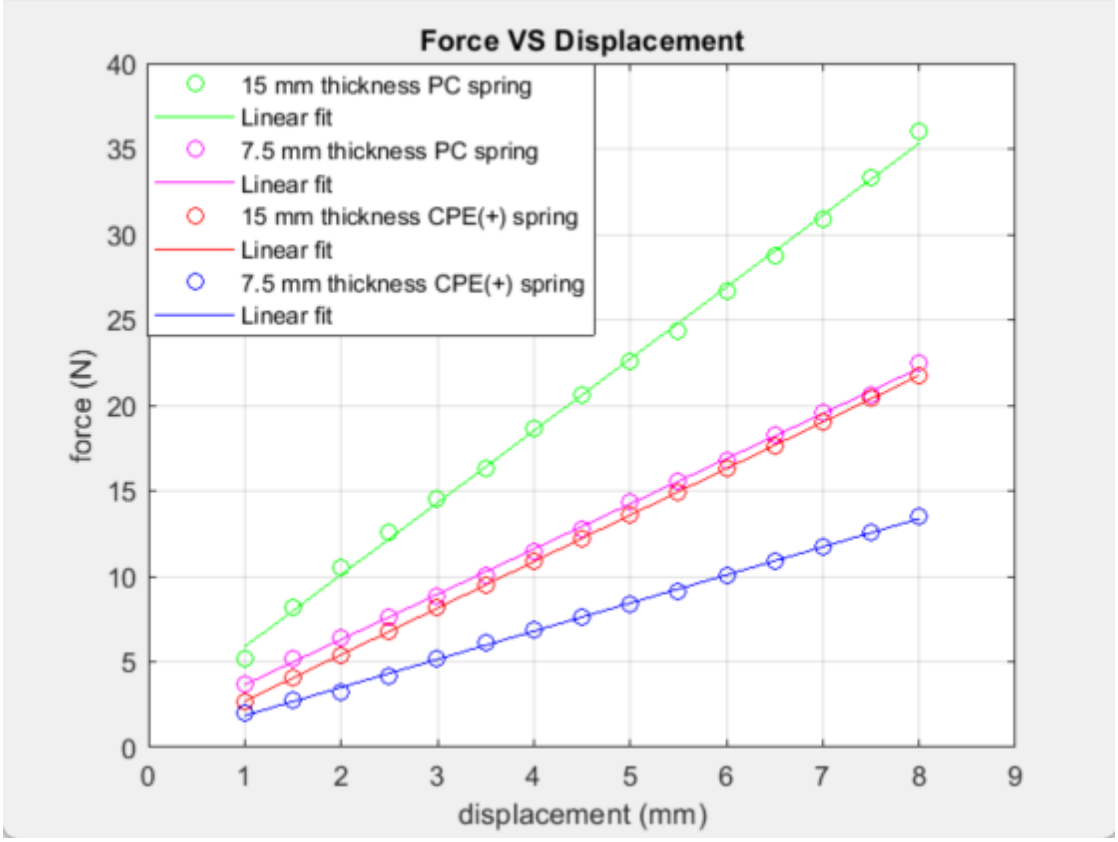

Figure 5.4: Force vs displacement graph for the CPE(+) and PC material-based ohm-shaped springs

For the CPE(+) material-based spring, two thicknesses were tested: 15 mm and 7.5 mm. The Simulated spring stiffness constant from the simulation, was found by comparing the displacement graph obtained as shown in Figure 5.5 and Figure 5.6. The ideal spring stiffness for a 15 mm thick spring is 2.85 N/mm and for a 7.5 mm thick spring is 1.81 N/mm. The calculated stiffness constant k_s from the experiment for the 15mm thick spring was found to be 2.74 N/mm. For the 7.5 mm thick spring, the stiffness constant k_s was measured as 1.64 N/mm. These results are graphically presented in Figure 5.4, where the force versus displacement for each spring is plotted.

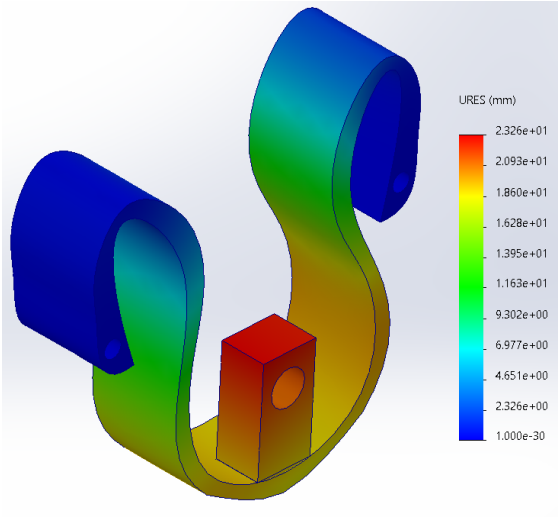

Figure 5.5: Displacement plot of 15 mm thickness CPE(+) Ω-shaped spring

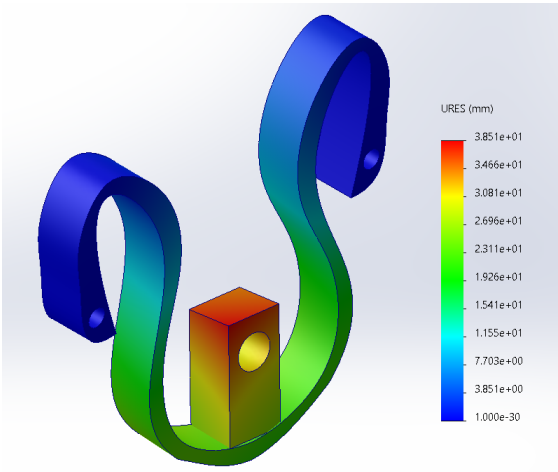

Figure 5.6: Displacement plot of 7.5 mm thickness CPE(+) Ω-shaped spring

In the case of the PC material-based spring, the simulated spring stiffness constant from the simulation, was found by comparing the displacement graph obtained as shown in Figure 5.7 and Figure 5.8. The simulated spring stiffness for a 15 mm thick spring is 4.44 N/mm and for a 7.5 mm thick spring is 2.73 N/mm. The calculated stiffness constant k_s from the experiment for the 15mm thick spring was found to be 4.21 N/mm. For the 7.5 mm thick spring, the stiffness constant k_s was measured as 2.64 N/mm. These results are graphically presented in Figure 5.4, where the force versus displacement for each spring is plotted.

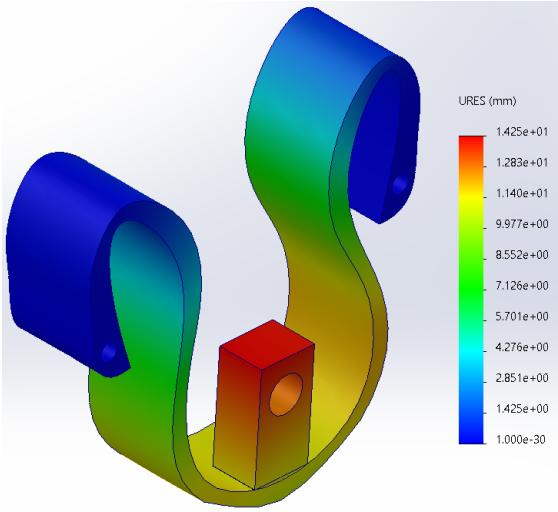

Figure 5.7: Displacement plot of 15 mm thickness PC Ω-shaped spring

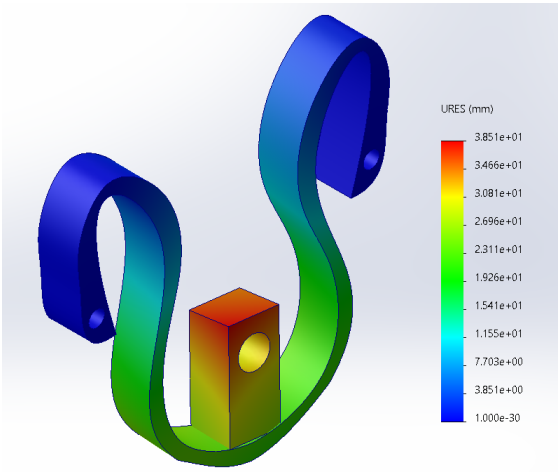

Figure 5.8: Displacement plot of 7.5 mm thickness PC Ω-shaped spring

It can be seen from Figure 5.4 demonstrates a linear behavior but does not pass through the origin, potentially due to initial pre-stress in the spring or systematic measurement errors. The subsequent sections will discuss the analysis and implications of these findings.

5.4 Output Stiffness of developed VIA

Understanding the dependence of the output stiffness of a lever-arm-based VIA on the length of the lever and the distance of the pivot from the free end of the lever is crucial, as indicated

in reference 4.1.6.

In the VIA under study, the lever set-point position is regulated by the outer coaxial shaft of the multi-axis motor. This shaft initiates the rotation of the frame, leading to the adjustment of the lever to the desired location. It is noted that the torque exerted on the lever primarily stems from the external load, which engenders a force due to gravity acting on the output shaft, affixed to the free end of the lever. For evaluation purposes, it is a valid assumption to interpret the torque enacted on the load-bearing end of the lever as a normal load. Thus, the output stiffness is computed based on this normal force (effectively the output force acting on the lever) and the deflection induced in the spring by this force.

An experiment was designed such that the lever was positioned parallel to the horizontal plane, thereby facilitating a normal vertical load to exert an input force on the lever. Figure 5.9 shows the experimental setup of evaluating the output stiffness of the designed VIA.

The theoretical output stiffness constant of the mechanism can be calculated based on the equation 4.1.3. By plotting output force F_o vs the deflection of the spring, the stiffness constant at each pivot position can be determined.

The following procedure was adopted for measuring the output stiffness:

1. Initially, the pivot is set to a zero position, and a load beginning from 10 grams is hung on the lever's free end.
2. The load is measured for every 1mm of deflection at the set pivot point. A vernier caliper is employed to measure the spring's deflection.
3. This process is iterated for various pivot positions, specifically for every 10mm change in the pivot position from its initial location.
4. By plotting a graph of Force VS Deflection the output stiffness 'K' can be identified for each pivot position.
5. Using equation 4.1.3, a mathematical model was developed, and simulations were conducted in MATLAB. This provided an estimate of the theoretical stiffness range for the VIA. These theoretical values were subsequently compared with the actual experimental results.

The outlined procedure was employed to determine the range of stiffness provided by the VIA for CPE(+) and PC spring. Figure 5.10 illustrates the theoretical and experimental range of stiffness generated by the VIA incorporating a CPE(+) material-based spring.

(a) 0mm pivot position **(b)** 10mm pivot position **(c)** 20mm pivot position

(d) 30mm pivot position **(e)** 40mm pivot position

Figure 5.9: Expeimental setup to identify the range of stiffness of the developed multi-axis integrated VIA at different pivot positions

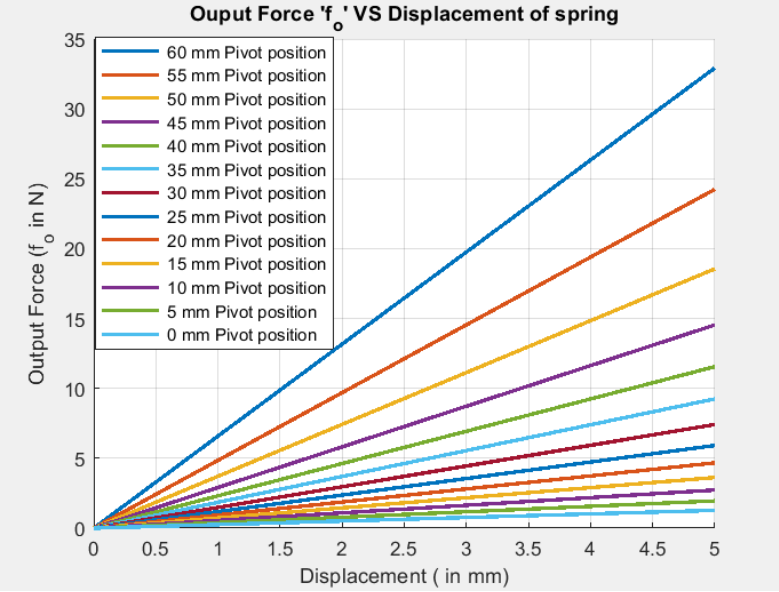

(a) Theoretical stiffness range CPE(+) spring based VIA

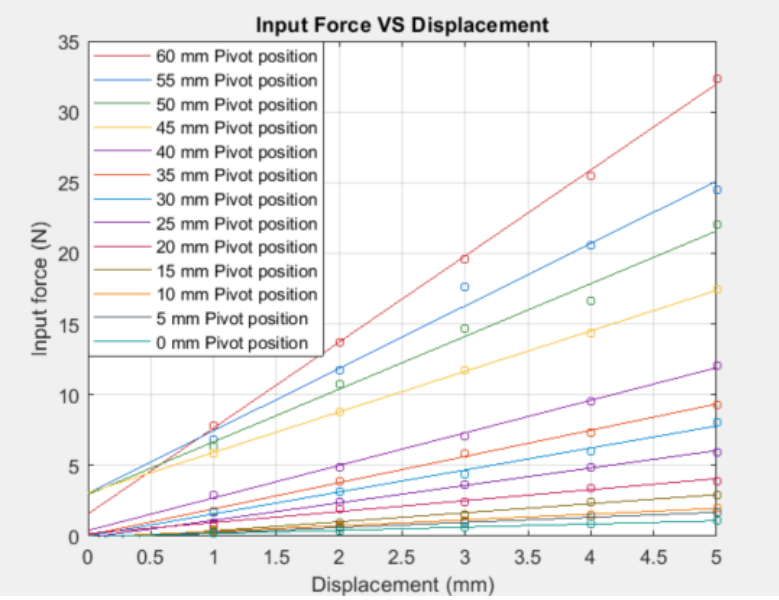

(b) Experimental Stiffness range CPE(+) spring based VIA

Figure 5.10: Force vs Displacement graph of VIA utilizing a CPE(+) material-based spring

A notable observation from the graph is the significant variation in the stiffness of the VIA with changes in pivot points. The stiffness constant 'K' of the VIA for each pivot position is summarised in Table 5.1. These stiffness constants were calculated by determining the slope

of the graph.

Table 5.1: Comparison of Theoretical and Experimental Stiffness of CPE(+) spring based VIA

Pivot Position (mm)	Theoretical (N/mm)	Experimental (N/mm)	Relative Error (%)
0	0.25	0.22	12.00
5	0.39	0.36	7.69
10	0.55	0.44	20
15	0.72	0.64	11.11
20	0.93	0.77	17.18
25	1.18	1.23	4.24
30	1.48	1.55	4.73
35	1.85	1.85	0.00
40	2.31	2.30	0.43
45	2.91	2.86	1.72
50	3.71	3.73	0.54
55	4.85	4.41	9.07
60	6.59	5.98	9.26

Similarly in the case of PC spring-based VIA Figure 5.11 illustrates the theoretical and experimental range of stiffness generated by the VIA.

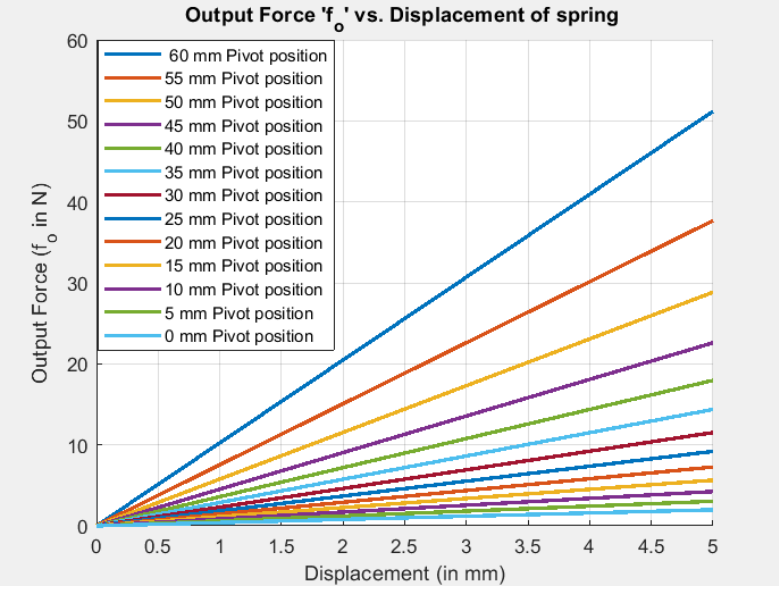

(a) Theoretical stiffness range PC spring based VIA

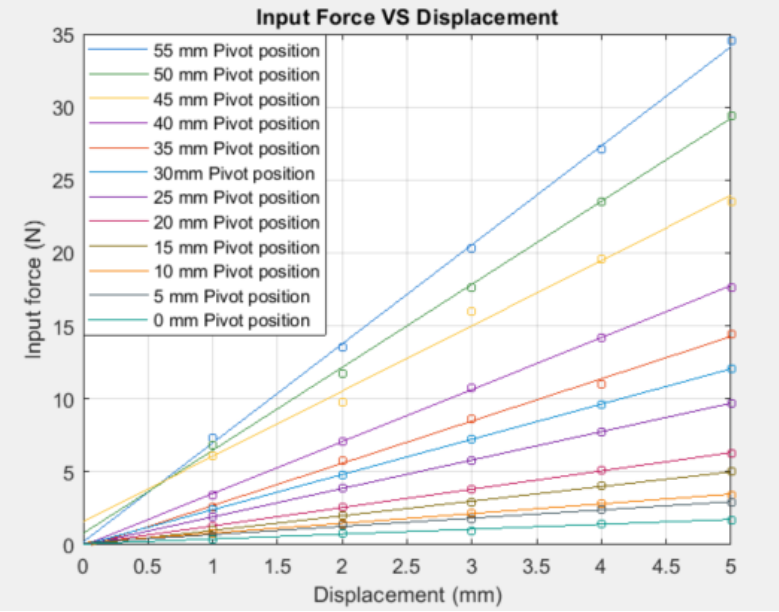

(b) Experimental Stiffness range PC spring based VIA

Figure 5.11: Force vs Displacement graph of VIA utilizing a PC material-based spring

The stiffness constant, denoted as 'K', for each pivot position in the VIA is presented in Table 5.1. Experimental data for a pivot position of 60 mm was intentionally excluded to prevent potential damage to the mechanism under excessive load.

Table 5.2: Comparison of Theoretical and Experimental Stiffness of PC spring-based VIA

Pivot Position (mm)	Theoretical (N/mm)	Experimental (N/mm)	Relative Error (%)
0	0.40	0.34	14.73
5	0.61	0.56	7.63
10	0.8	0.69	13.75
15	1.13	1.00	11.61
20	1.45	1.20	17.42
25	1.84	1.74	5.51
30	2.30	2.20	4.51
35	2.87	2.87	0.27
40	3.59	3.58	0.28
45	4.52	4.49	0.69
50	5.77	5.70	1.22
55	7.54	6.79	9.96
60	10.24	-	-

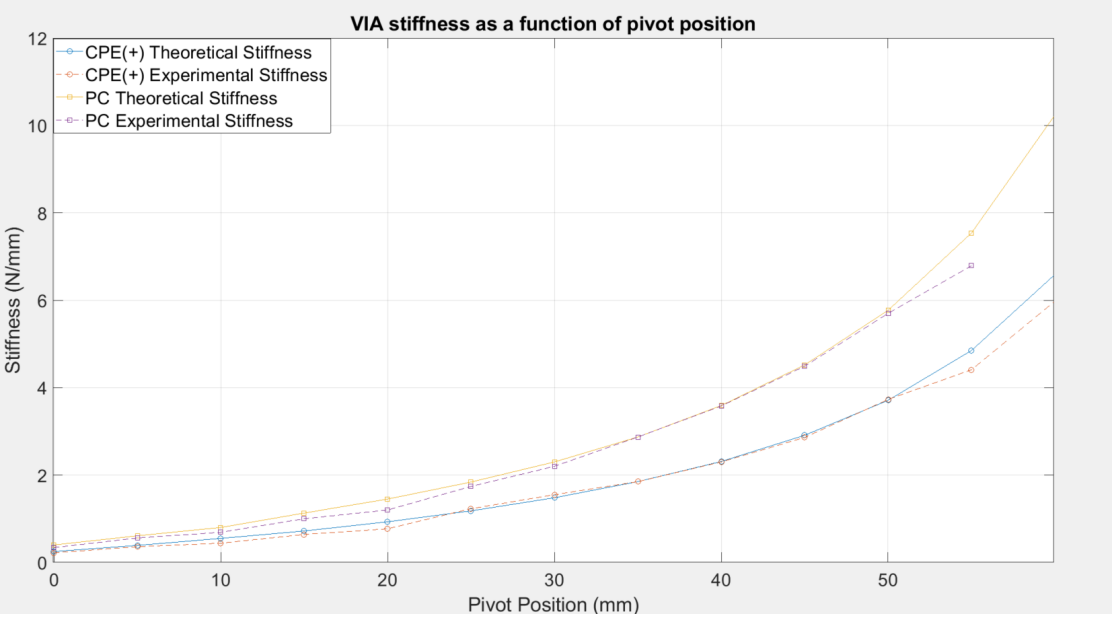

Figure 5.12: Comparison of stiffness of the developed VIA

Figure 5.12 visualizes the data from Tables 5.1 and 5.2. It illustrates the range of stiffness achieved by various VIA variants in relation to the pivot position of the developed VIA. Addi-

tionally, this figure allows for a comparison between the theoretical and experimental stiffness values.

5.5 Discussions

This section aims to concisely delve deeper into evaluations and results obtained from the experimentations performed on the multi-axis integrated VIA.

5.5.1 Motor Results

Preliminary experiments were conducted to highlight the advancements in the multi-axis motor. The comparison of the motor torque constant, obtained by directing the motor's full power to individual rotors separately, not only aids in understanding motor improvements but also establishes a framework for comparisons across different configurations, as demonstrated in [33]. Although the current design features only 2 rotors, in contrast to the 3-rotor configuration of its predecessor, the motor torque constant remains an effective method for direct comparison, bridging the structural differences.

As highlighted in section 5.1, the 50-teeth rotor has a motor torque constant of 0.18N/m, which is 33% higher than the maximum achieved by the 46-teeth rotor of the 3-axis motor. Figure 5.2 further shows the capability of the current multi-axis motor to produce a peak torque of 0.34Nm at 1.3 A current with the 50-teeth rotor, in contrast to the 0.15Nm at 1.1 A current from the 46-teeth rotor of the 3-axis motor. The increase in torque from 0.150Nm to 0.31Nm can be attributed to the combined effects of the increased number of teeth, the larger rotor size, and the additional stator windings for each phase. The 33% increase in the motor torque constant accounts for some portion of this torque improvement, while the combined factors provide the remainder of the enhancement.

However, the torque of the outer axial shaft with 51 teeth rotor could not be found due to the mechanical frictions present in the current motor. This is possibly due to a manufacturing error as the top bearing housing sits tightly over the outer shaft of the multi-axis motor. This can be eliminated by increasing the bore to ensure there is no contact between the casing and the shafts themselves. Ideally, it is expected that the torque of the 51-teeth rotor must be similar to that of the 50-teeth rotor because both rotors have the same dimension except for the teeth difference.

Similarly from section 5.2 the maximum rotor speed of the 50 teeth rotor is 1100 RPM, which is significantly lower when compared to the maximum speed attained by the rotor of the most

number of teeth of the 3-axis motor. This reduction in speed is expected due to the trade-off of achieving increased torque. Also the increase in the number of teeth and the height of the rotor while keeping the diameter constant can have a negative effect on the no-load speed of the motor because this increase improves the precision, thereby allowing the motor to have a very small step. However, it is worth noting that due to the existing frictional forces, it also affects the maximum attainable no-load speed of the motor.

5.5.2 Spring Stiffness Results

In the design and functionality of the VIA, the stiffness of the Ω-shaped springs influences directly the output stiffness of the VIA itself. Therefore, a detailed understanding of these springs and the factors affecting their stiffness becomes paramount.

The Ω-shaped springs, as depicted in Figure 5.4, consistently demonstrate linear characteristics across different materials used.

Experimental Data: The inherent mechanical properties of the materials largely define the stiffness differences. For the 15mm thickness, the CPE(+) springs, with Young's modulus of 1.52 GPa, exhibit a stiffness of 2.74N/mm. In contrast, the PC springs, with Young's modulus of 2.64 GPa, display a stiffness of 4.21N/mm. When the thickness is reduced to 7.5mm, the stiffness values are 1.64N/mm for CPE(+) and 2.64N/mm for PC.

Simulation Data: Simulation results provide slightly different values. For the 15mm thickness springs, the stiffness values are 2.85N/mm for CPE(+) and 4.37N/mm for PC. For the 7.5mm thickness springs, the stiffness values are 1.75N/mm for CPE(+) and 2.72N/mm for PC.

The one significant factor contributing to the discrepancy between the experimental and simulation data is the nature of the 3D-printed material. 3D printed materials are not completely solid due to the layer-by-layer deposition process and possible micro-voids, which can influence mechanical properties. On the other hand, simulations often consider materials as entirely solid, leading to variations in the predicted outcomes. Other factors that could result in discrepancies include material inconsistencies, boundary conditions in the simulation, and measurement errors in the experimental setup.

From Equation 2.1.1 the relationship is evident in both the experimental and simulated data, where a reduction in thickness leads to a significant decline in stiffness. Table 5.3 provides a comprehensive summary of the characteristics of the Ω-shaped springs for quick reference.

These experimental results provide a comparative understanding of the spring's stiffness in terms of the different materials and thicknesses. From, the simulation and experimentation

Table 5.3: Material properties and spring stiffness of CPE(+) and PC springs

Material	Tensile Strength (MPa)	Young's Modulus (GPa)	Thickness (mm)	Spring Stiffness (Experimental) (N/mm)	Spring Stiffness (Simulated) (N/mm)
CPE(+)	48	1.52	15	2.74	2.85
			7.5	1.64	1.75
PC	68	2.64	15	4.21	4.37
			7.5	2.64	2.72

results as highlighted in Table 5.3, the 7.5mm thick Ω-shaped spring is most suitable for the developed VIA.

5.5.3 Output Stiffness of developed VIA

In evaluating the performance of the multi-axis motor-integrated VIA, determining the range of available stiffness is crucial.

To ensure uniform movements during testing and to eliminate potential positioning errors from manual settings, the pivot was manipulated using the multi-axis motor under feedforward control. Given the interconnected nature of the entire VIA frame and the outer shaft, this method substantially reduced system-wide vibrations, thus enhancing the accuracy of the results. This methodology offered a controlled setting for an exhaustive evaluation of the concept.

Figure 5.10b and Figure 5.11b illustrate the output stiffness shows significant variation with changes in the pivot position. Specifically, the force required to linearly deflect the Ω-shaped spring differs for various pivot points, corroborating the relationship depicted in Equation 4.1.6.

From the experimental data in Table 5.1, the lowest stiffness constant observed for the CPE(+) spring-based VIA is 0.22 N/mm. This is significantly lower than the stiffness of the Ω-shaped spring crafted from CPE+. Conversely, the highest achievable stiffness is 5.98 N/mm, substantially exceeding the stiffness of the aforementioned spring. These observations reinforce the notion that output stiffness is predominantly influenced by the transmission ratio set by the pivot's position. For the PC spring-based VIA, the stiffness range spans from 0.34 N/mm at the lowest to approximately 10 N/mm at its peak, mirroring the trend observed in the CPE(+) spring-based VIA. However, the total stiffness range of the PC spring-based VIA is broader than its CPE(+) counterpart.

A comparison of the theoretical and experimental stiffness ranges for both VIA variants is illustrated in Figure 5.10a and Figure 5.11a. The experimental data closely mirrors the theoretical model, with minor discrepancies at the starting points. These discrepancies can be attributed to pre-existing spring stress and systematic measurement errors, indicating an initial load

responsible for the variation. Notably, both the CPE(+) and PC spring-based VIAs exhibit comparable trends, helping demonstrate the behavior of the developed VIA.

Upon comparing the theoretical and experimental stiffness constants at each pivot point, as depicted in Figure 5.12, it is evident that the change in stiffness with the pivot position is non-linear for both sets of data. This observation holds true even though the spring displays linear characteristics. This indicates that the lever arm mechanism with a movable pivot point plays a pivotal role in the change in stiffness of the developed VIA. Many of the experimental values align closely with the theoretical predictions. However, between pivot positions of 25-35 mm, the experimental values exceed the theoretical ones. A closer examination reveals that the pivot is not adequately constrained in these positions. Even when the pivot position remains constant, it bends under load. This bending effect is particularly pronounced in the mid-range of the pivot positions. Moreover, the gap between the experimental and theoretical values seems to widen as the pivot approaches the loading point, specifically between 45-60 mm. This divergence can be attributed to the bending of the pivot stabilizer under high loads, which results from increased stiffness and subsequently affects the overall system stiffness.

It's worth noting that the highest relative error, approximately 17%, consistently appears at the 20 mm pivot position. Aside from these specific cases, the observed values largely concur with the theoretical model. Starting from the 30 mm pivot position, there's a distinct shift in the stiffness constant. This underscores the significant influence internal loads have on determining output stiffness relative to pivot point adjustments. As a result, a lower pivot position necessitates less torque for lever deflection and vice versa. This characteristic underscores the VIA system's capacity to fine-tune its stiffness, demonstrating its adaptability.

Chapter 6

Conclusion and Recommendation

6.1 Conclusion

This research embarked on an exploration to address the intricate challenge of integrating multi-axis motors with Variable Impedance Actuators (VIAs). The developed model not only confirms the feasibility of such an integration but also underscores the potential advancements in actuator efficiency, adaptability, and precision. Initially, the study focuses on identifying the different categories of VIAs and understanding the strengths and weaknesses of each category. Drawing from systematic literature, it was observed that the lever arm-based mechanism as an optimal choice for a VSA-type VIA. The primary categories of VIAs include active impedance by control, Inherent Damping, and Inertial VIAs, as depicted in Figure 2.1. Building on these insights, it was found that a concentric two-axis motor can adeptly control both the spring stiffness and the motor setpoint angle. This holds particularly true for VIAs in the "inherent compliance" category, more specifically the "Adjusting load-spring transmission ratio" type.

In addressing the research challenge of enhancing the torque of a multi-axis motor for optimal integration with a Variable Impedance Actuator, this study presents several pivotal findings. Transitioning from a 3-rotor to a 2-rotor configuration led to discernible performance enhancements. The 50-teeth rotor demonstrated a motor torque constant of 0.18 Nm/A as shown in Figure 5.2, marking a 33% improvement over the 46-teeth rotor from the 3-axis configuration. In terms of maximum achievable torque, the 50-teeth rotor reached a peak of 0.34 Nm (Figure 5.2), significantly outperforming the 0.15 Nm generated by its 3-axis counterpart. This torque increase is a cumulative effect of the rotor's larger size, increased number of teeth, and the subsequent increase in stator windings. While the motor torque constant's augmentation was

instrumental, it's the integration of these design changes that provided the substantial boost in torque, optimizing the motor's integration with the Variable Impedance Actuator. However, these benefits come with an inherent trade-off: the motor's maximum speed reached only about 1100 RPM during no-load conditions at a maximum voltage of 15 V. Furthermore, while the increased torque is a positive indicator, it doesn't provide a comprehensive view of the motor's overall efficiency. Friction within the system, especially evident in the outer shaft with the 51-teeth rotor, counteracts some of the torque gains.

Another significant outcome of the research was the introduction of the Ω-shaped spring, fabricated from engineering plastics. This unique design offers multiple advantages: it provides a linear behavior profile, has a stiffness comparable to conventional metal springs, and is lighter. This makes it particularly suited for streamlined manufacturing processes.

Experiments detailed in section 5.3 revealed the spring constants for different variants. The 15mm thick spring for CPE(+) exhibited a spring constant of 2.74 N/mm, while its 7.5mm thick counterpart showed a spring constant of 1.64N/mm. For PC springs, the 15mm thickness resulted in a spring constant of 4.21N/mm, and the 7.5mm thickness exhibited 2.64N/mm. It was discerned that the 7.5mm thick spring, irrespective of material choice, proved to be the most suitable for the developed VIA, achieving the desired balance between compliance and stiffness.

When comparing the stiffness range of the VIA with different springs, the CPE(+) spring-based VIA showed in Figure 5.10b a range from 0.22N/mm to 5.98 N/mm. On the other hand, the PC spring-based VIA ranged from 0.34 N/mm to roughly 10N/mm, as illustrated in Figure 5.11b. These empirical outcomes are consistent with our mathematical predictions, presenting an average deviation of around 8%. These results emphasize the influential role of both material and shape in determining the stiffness range.

The developed controller for the multi-axis motor, depicted in Figure 3.4, allows users to adjust both the velocity and position of the motor. A key feature is the feed-forward control, designed to set the pivot point position, thus modulating the stiffness of the multi-axis VIA. Users can set the pivot position using the "Pivot point slider" in the Matlab UI (Figure 4.14), and specify the lever position via the "motor control" tab (Figure 4.12). This design facilitates the optimization of both stiffness and position control using a single controller individually by the user. However, the absence of a feedback loop means the system can't recalibrate position errors, and simultaneous control over stiffness and position is currently not possible. For the current model, the initial position must be manually calibrated by the user.

Furthermore, a notable observation during the evaluation was the multi-axis motor's thermal

performance. Despite extended testing durations, the motor remained within acceptable temperature limits, ensuring longevity and reliability in real-world applications. This thermal stability further attests to the viability of the developed integration, making it suitable for prolonged and intensive tasks.

In conclusion, the achieved integration between the VIAs and the multi-axis motor has successfully enhanced actuator precision. Moreover, the design indicates a potential reduction in system complexities, suggesting that future actuator systems might benefit from a single-control architecture. It is evident that this study serves as a foundational platform, guiding future endeavors in the creation of efficient passive-compliant VIA systems powered by multi-axis motors.

6.2 Recommendations

The present model concentrates on the development of a lever-arm-based VIA using a multi-axis motor. This decision was based primarily on the advantages of the lever-arm design given the specific constraints of the multi-axis motor. However, this does not imply that other VIA types are infeasible with a multi-axis motor. Future research could explore these alternatives, using the current model as a benchmark for the multi-axis motor's utilization.

The current model only provides a feedforward control technique due to pragmatic reasons and time constraints. The control mechanism can be improved by incorporating a feedback loop. This addition could create an opportunity to develop a controller that adjusts the stiffness in response to forces from the external environment. Incorporating force sensors into the design would be a practical way to create this feedback loop, enabling real-time responsiveness to changes in external forces. Additionally, with respect to the motor design, further research can focus on reducing overall heat dissipation.

Furthermore, as this is the first iteration using a multi-axis motor, the size of the current design is relatively large. Future iterations could aim to develop a more compact yet efficient VIA. This would increase its versatility and application potential, making it more suitable for a wider range of uses.

A detailed study could be conducted to evaluate the energy consumption of the VIA model with the multi-axis motor. This would help in designing more energy-efficient systems, extending operational time, and reducing overall costs.

References

1. Ham, R. V., Sugar, T. G., Vanderborght, B., Hollander, K. W. & Lefeber, D. Compliant actuator designs. *IEEE Robotics & Automation Magazine* **16,** 81–94 (2009).
2. Hu, W., Li, W. & Alici, G. *3D Printed Helical Soft Pneumatic Actuators* in *2018 IEEE/ASME International Conference on Advanced Intelligent Mechatronics (AIM)* (2018), 950–955.
3. Do, B. H., Choi, I. & Follmer, S. An All-Soft Variable Impedance Actuator Enabled by Embedded Layer Jamming. *IEEE/ASME Transactions on Mechatronics* **27,** 5529–5540 (2022).
4. Vanderborght(2012), B. *et al. Variable impedance actuators: Moving the robots of tomorrow* in *2012 IEEE/RSJ International Conference on Intelligent Robots and Systems* (2012), 5454–5455.
5. Berret, B., Sandini, G. & Nori, F. *Design principles for muscle-like variable impedance actuators with noise rejection property via co-contraction* in *2012 12th IEEE-RAS International Conference on Humanoid Robots (Humanoids 2012)* (2012), 222–227.
6. Vanderborght(2013), B. *et al.* Variable Impedance Actuators: a Review. English. *Robotics and Autonomous Systems* **61,** 1601–1614. ISSN: 0921-8890 (Dec. 2013).
7. Albu-Schäffer, A. *et al.* The DLR lightweight robot: design and control concepts for robots in human environments. *Industrial Robot: an international journal* **34,** 376–385 (2007).
8. Josephine Selvarani Ruth, D. & Dhanalakshmi, K. Role of Shape Memory Alloy Wires as a SENSAPTIC HMI Device. *IEEE Sensors Journal* **20,** 6422–6431 (2020).
9. Nelson, C. A., Nouaille, L. & Poisson, G. *Variable stiffness mechanism for robotic rehabilitation* in *Advances in Mechanism and Machine Science: Proceedings of the 15th IFToMM World Congress on Mechanism and Machine Science 15* (2019), 1761–1769.
10. Nahar, D. & Sugar, T. *Compliant constant-force mechanism with a variable output for micro/macro applications* in *2003 IEEE International Conference on Robotics and Automation (Cat. No.03CH37422)* **1** (2003), 318–323 vol.1.

11. Bicchi, A. & Tonietti, G. Fast and" soft-arm" tactics [robot arm design]. *IEEE Robotics & Automation Magazine* **11,** 22–33 (2004).
12. Bicchi, A., Tonietti, G., Bavaro, M. & Piccigallo, M. *Variable stiffness actuators for fast and safe motion control* in *Robotics Research. The Eleventh International Symposium: With 303 Figures* (2005), 527–536.
13. Pratt, G. A. & Williamson, M. M. *Series elastic actuators* in *Proceedings 1995 IEEE/RSJ International Conference on Intelligent Robots and Systems. Human Robot Interaction and Cooperative Robots* **1** (1995), 399–406.
14. Grebenstein, M. *et al. The DLR hand arm system* in *2011 IEEE International Conference on Robotics and Automation* (2011), 3175–3182.
15. Tsagarakis, N. G., Sardellitti, I. & Caldwell, D. G. *A new variable stiffness actuator (CompAct-VSA): Design and modelling* in *2011 IEEE/RSJ International Conference on Intelligent Robots and Systems* (2011), 378–383.
16. Wolf, S. *et al.* Variable Stiffness Actuators: Review on Design and Components. *IEEE/ASME Transactions on Mechatronics* **21,** 2418–2430 (2016).
17. Rodriguez-Cianca, D. *et al.* A variable stiffness actuator module with favorable mass distribution for a bio-inspired biped robot. *Frontiers in neurorobotics* **13,** 20 (2019).
18. Guo, J. & Tian, G. Mechanical design and robust tracking control of a class of antagonistic variable stiffness actuators based on the equivalent nonlinear torsion springs. *Proceedings of the Institution of Mechanical Engineers, Part I: Journal of Systems and Control Engineering* **232,** 1337–1355 (2018).
19. Cifuentes, C. A. *et al.* Variable stiffness actuators for wearable applications in gait rehabilitation. *Interfacing Humans and Robots for Gait Assistance and Rehabilitation,* 193–212 (2022).
20. Malosio, M., Spagnuolo, G., Prini, A., Tosatti, L. M. & Legnani, G. Principle of operation of RotWWC-VSA, a multi-turn rotational variable stiffness actuator. *Mechanism and Machine Theory* **116,** 34–49 (2017).
21. Van Ham, R., Vanderborght, B., Van Damme, M., Verrelst, B. & Lefeber, D. MACCEPA, the mechanically adjustable compliance and controllable equilibrium position actuator: Design and implementation in a biped robot. *Robotics and Autonomous Systems* **55,** 761–768 (2007).
22. Visser, L., Carloni, R., Ünal, R. & Stramigioli, S. *Modeling and design of energy efficient variable stiffness actuators* in *2010 IEEE International Conference on Robotics and Automation* (2010), 3273–3278.

23. Jafari, A., Tsagarakis, N. G. & Caldwell, D. G. A novel intrinsically energy efficient actuator with adjustable stiffness (AwAS). *IEEE/ASME transactions on mechatronics* **18,** 355–365 (2011).
24. Jafari, A., Tsagarakis, N. G. & Caldwell, D. G. *AwAS-II: A new actuator with adjustable stiffness based on the novel principle of adaptable pivot point and variable lever ratio* in *2011 IEEE International Conference on Robotics and Automation* (2011), 4638–4643.
25. Tsagarakis, N. G., Sardellitti, I. & Caldwell, D. G. *A new variable stiffness actuator (CompAct-VSA): Design and modelling* in *2011 IEEE/RSJ International Conference on Intelligent Robots and Systems* (2011), 378–383.
26. Groothuis, S. S., Rusticelli, G., Zucchelli, A., Stramigioli, S. & Carloni, R. *The vsaUT-II: A novel rotational variable stiffness actuator* in *2012 IEEE International Conference on Robotics and Automation* (2012), 3355–3360.
27. Fumagalli, M., Barrett, E., Stramigioli, S. & Carloni, R. *The mVSA-UT: A miniaturized differential mechanism for a continuous rotational variable stiffness actuator* in *2012 4th IEEE RAS & EMBS International Conference on Biomedical Robotics and Biomechatronics (BioRob)* (2012), 1943–1948.
28. Jafari, A., Tsagarakis, N. G., Sardellitti, I. & Caldwell, D. G. *How design can affect the energy required to regulate the stiffness in variable stiffness actuators* in *2012 IEEE International Conference on Robotics and Automation* (2012), 2792–2797.
29. Barrett, E., Fumagalli, M. & Carloni, R. *Elastic energy storage in leaf springs for a lever-arm based Variable Stiffness Actuator* in *2016 IEEE/RSJ International Conference on Intelligent Robots and Systems (IROS)* (2016), 537–542.
30. Kahlen, K., Voss, I., Priebe, C. & De Doncker, R. Torque control of a spherical machine with variable pole pitch. *IEEE Transactions on Power Electronics* **19,** 1628–1634 (2004).
31. Uygun, D., Solmaz, S., Turan, A. & Ruzgar, S. T. *A new topology for dual rotor/stator BLDC motors applied to marine thrusters* in *2015 IEEE 5th International Conference on Power Engineering, Energy and Electrical Drives (POWERENG)* (2015), 353–359.
32. Xu, L. *et al.* Orthogonal Magnetic Field Analysis of a Double-Stator Linear-Rotary Permanent Magnet Motor With Orthogonally Arrayed Permanent Magnets. *IEEE Transactions on Magnetics* **53,** 1–4 (2017).
33. Groenhuis, V., Rolff, G., Bosman, K., Abelmann, L. & Stramigioli, S. Multi-axis electric stepper motor. *IEEE Robotics and automation letters* **6,** 7201–7208 (2021).
34. Groenhuis, V., Rolff, G., Bosman, K., Abelmann, L. & Stramigioli, S. *Absolute Position Detection in 7-Phase Sensorless Electric Stepper Motor* in *2022 IEEE/RSJ International Conference on Intelligent Robots and Systems (IROS)* (2022), 3115–3122.

35. Muetstege, C. *Demonstration of a multi-axis stepper motor in a robotic system* 2022. http://essay.utwente.nl/89747/.
36. Yigit, C. B., Bayraktar, E. & Boyraz, P. Low-cost variable stiffness joint design using translational variable radius pulleys. *Mechanism and Machine Theory* **130,** 203–219 (2018).
37. Xu, Y., Guo, K., Sun, J. & Li, J. Design, modeling and control of a reconfigurable variable stiffness actuator. *Mechanical Systems and Signal Processing* **160,** 107883 (2021).
38. Yang, Z. *et al.* Dynamic performance analysis of the variable stiffness actuator considering gap and friction characteristics based on two-inertia-system. *Mechanism and Machine Theory* **168,** 104584 (2022).
39. Sun, Y. *et al.* Modeling and Experimental Evaluation of a Pneumatic Variable Stiffness Actuator. *IEEE/ASME Transactions on Mechatronics* **27,** 2462–2473 (2022).
40. Martins, L. T. *et al. Polyurethane-based modular series elastic upgrade to a robotics actuator* in *RoboCup 2015: Robot World Cup XIX 19* (2015), 347–355.
41. *Ultimaker MakerBot Support Center* https://support.makerbot.com/s/article/1667337600364. Accessed: July 19, 2023.
42. Edge, E. *Planetary Epicyclic Gear Ratios Equations and Calculators* Accessed: 2023-07-20. 2023. https://www.engineersedge.com/gears/planetary_epicyclic_gear_13736.htm.
43. Lopez, J. P. *DEMONSTRATION OF MULTI-AXIS STEPPER MOTOR IN 2-DOF MARBLE-MAZE APPLICATION* (2023).